Fuel Processing Technology 231 (2022) 107231

Contents lists available at ScienceDirect

Fuel Processing Technology

journal homepage: www.elsevier.com/locate/fuproc

On the evolution of n-octane atomization characteristics using an air-assisted intermittent spray method

Hao Wu [a,b], Fujun Zhang [a], Zhenyu Zhang [a,b,*], Kun Wu [c], Xuejun Fan [c]

[a] School of Mechanical Engineering, Beijing Institute of Technology, Beijing 100081, China
[b] Yangtze Delta Region Academy of Beijing Institute of Technology, Jiaxing 314011, Zhejiang, China
[c] State Key Laboratory of High Temperature Gas Dynamics, Institute of Mechanics, Chinese Academy of Sciences, Beijing 100190, China

ARTICLE INFO

Keywords:
Air-assisted spray
Droplet size-velocity joint probability density function
Sauter Mean Diameter
Turbulent intensity
Slip velocity

ABSTRACT

In this study, droplet size and velocity of an intermittent air-assisted n-octane spray were measured using a Phase Doppler Particle Analyzer, focusing on the effect of operating parameters on time-resolved droplet behavior and local gas flow characteristics. An electro-magnetically actuated air-assisted injector, which features internal gas-liquid premixing upstream and releasing through an annular nozzle, was used to generate intermittent sprays. The sampling time equalization method is employed to examine the time-resolved spray microscopic characteristics with various injection control parameters and spatial sampling positions. The droplet diameter range is found to be generally independent of air injection duration and sampling time while droplet velocity is correlated with these two parameters. A large air injection duration tends to accelerate droplets in the late spray period and leads to an increasing normalized gas flow velocity. Estimation of local gas flow turbulence intensity indicates a prominent radial sampling position dependence due to the rapid attenuation of the gas flow velocity away from the spray axis. A noteworthy finding for this intermittent air-assisted spray is that at 30 mm from the nozzle outlet, the zero point of droplet-gas mean slip velocity shifts toward the nozzle with sampling time. The time bin size employed to divide the sampling time has been proved to exert no influence on the statistical results of transient spray microscopic characteristics.

1. Introduction

Liquid atomization can generally be classified into single-fluid types and twin-fluid types depending on the type of fluids involved [1,2]. The single-fluid atomization method is simple in terms of the implementation principle and has been widely adopted in automotive fuel injection systems. However, the improvement of single-fluid atomization depends much on the establishment of the sufficiently high fluid potential or nozzle configuration optimization [3–5]. For twin-fluid atomization, an additional medium (pressurized gas) is usually employed to assist the liquid atomization [6]. This atomization method and resultant sprays essentially involve relatively complex multi-phase flow issues, especially considering the stochastic nature of carrier-phase (normally gas) turbulence and polydispersity of dispersed-phase (normally liquid) distribution [7,8]. The twin-fluid atomization can be further subdivided into internal mixing and external mixing types according to the position where the liquid and atomizing gas get contacted [6,9].

Featured design of internal mixing twin-fluid atomization is embodied in the fact that the gas and liquid come into contact and premix within the nozzle upstream before released [10]. This type of atomization method is characterized by the diversity of atomization implementation, the complexity of atomization mechanism due to multiscale and multiple instabilities, as well as its insensitivity to fluid properties [11–14]. With the participation of additional gas, the twin-fluid atomization inherently provides significant design flexibility in terms of fluid supply, inner flow, gas-liquid mixing, and injection organization [15]. Therefore, the practical atomization of a twin-fluid spray can be influenced by a variety of factors, including the size, construction, and number of liquid (gas) nozzles, the properties of the fluids involved, the operating conditions, and injection pressure of the liquid and gas [16]. As a result, numerous prior investigations related to the twin-fluid atomization physics can be found to focus on the effects of nozzle geometry [6], effects of liquid properties [17], effects of system

Abbreviations: ASOT, after the start of trigger; Bin No., number of time bin; CVC, constant volume chamber; ECU, electronic control unit; JPDF, joint probability density function; PDPA, Phase Doppler Particle Analyzer; SMD, Sauter Mean Diameter.

* Corresponding author at: School of Mechanical Engineering, Beijing Institute of Technology, Beijing 100081, China.
E-mail address: zhenyu.zhang@bit.edu.cn (Z. Zhang).

https://doi.org/10.1016/j.fuproc.2022.107231
Received 4 January 2022; Received in revised form 18 February 2022; Accepted 28 February 2022
Available online 16 March 2022

Nomenclature

C_d	drag coefficient
C_v	coefficients of variation, dimensionless
D	droplet diameter, μm
E_x	measurement uncertainty, dimensionless
L	turbulence length scale
$L_{1/2}$	half width of jet/spray, mm
P	supply pressure, MPa
r	radial position, mm
S_E	standard error of droplet data
Stk	Stokes number, dimensionless
t	sampling time, ms
T_a	air injection duration, ms
T_{arrive}	time to reach measurement volume, ms
T_f	fuel injection duration, ms
T_i	fuel-air injection interval, ms
T_o	peak duration, ms
U	droplet velocity, m/s
U_T	droplet terminal velocity, m/s
U_m	mass-averaged velocity, m/s
U_{slip}	droplet-gas slip velocity, m/s
U_t	velocity of tracer droplet, m/s
u'	fluctuating velocity, m/s
u_r	standard deviation of carrier phase fluctuating velocity, m/s
x	axial position, mm
$\overline{x}$	arithmetic mean of droplet data rate
ΔT_{bin}	time bin size, ms

Greek symbols

μ	dynamic viscosity, kg/(m • s)
ν	kinematic viscosity, m^2/s
ρ	density, kg/m^3
σ	surface tension, N/m
σ_x	standard deviation of droplet data rate
τ	turbulence intensity, dimensionless
τ_0	droplet relaxation time
τ_t	turbulent time scale

Subscripts

g	atomizing gas (air)
i	index number of a droplet
l	atomized liquid (n-octane)
$r.\ m.\ s.$	root mean square

pressure and fluid velocity [18,19], effects of liquid and gas mass flow rate [20,21], etc.

Owing to recent advances in high-performance imaging as well as laser diagnostic technology, many ongoing attempts have been conducted to investigate the atomization mechanism, spray performance, and spray droplet behaviors in the areas involving both continuous and intermittent sprays [22]. When the operating conditions are fixed, steady atomization normally creates a continuous spray where the spray geometry, the spatial distribution of droplets, the droplet size and velocity hardly change over time [23]. Unlike continuous sprays which are commonly used in industrial and aerospace propulsion, piston-type internal combustion engines typically require injectors to operate intermittently to achieve pulsed injection, such as direct injectors in gasoline engines and common rail injectors in diesel engines [24–27]. At present, the principal approach for pulsed injection is to drive the needle valve inside the injector by electromagnetic force, thus performing quick and periodic switching between nozzle opening and closing [28,29]. Pulsed injection and resultant intermittent sprays typically operate for a duration less than 10 ms and are characterized by prominent transient and unsteady features [30]. These properties further complicate the atomization process and impose more stringent requirements for experimental measurements.

Extensive studies have been carried out to investigate pulsed injection and intermittent spray. Wang and his co-worker [31] investigated the macroscopic and microscopic characteristics of diesel spray using high-speed imaging and a Phase Doppler Particle Analyzer (PDPA) under both single injection and split-injection strategies. The results indicated that the split-injection strategy resulted in significant variations in spray characteristics under low temperature conditions and a strong droplet collision led to larger droplets. Moon et al. [32] characterized the velocity and turbulence intensity fields of the high-speed diesel sprays in the near-field using novel multi-exposed X-ray phase-contrast images (XPCI). They found spray deceleration is associated with the transfer of spray momentum to turbulence energy since the spray deceleration is coupled with the increase of the turbulence intensity. Their further investigation concerning the effects of governing parameters on the dynamics of turbulent spray atomization revealed that fuel and injection pressure promoted spray atomization but did not alter the spray dynamic structure [33]. Feng et al. [34] used particle/droplet image analysis (PDIA) to measure the droplet velocity and diameter distribution in the dilute region downstream of the pulsed diesel spray and obtained the statistical distribution. Analysis of droplet Stokes number and Weber number suggests that spray droplets are not intensely drifted by the gas flow that is induced by the momentum exchange with the droplets. Wu et al. [35] performed an experimental observation of pulsed hollow-cone sprays issuing from a voice coil motor injector and the results indicated the presence of a vortex-ring structure generated by flash boiling at the nozzle exit.

As a twin-fluid atomization method, air-assisted spray has attracted much attention in recent spray studies. Kourmatzis et al. [36] carried out extensive measurements on the momentum decay and droplet size of air-assisted liquid fuel sprays as a function of Reynolds number, mass loading, and spatial position. The results indicated that liquid break-up occurs in the near nozzle exit region, with minimal secondary atomization occurring further downstream. Manish and Sahu [37] paid more attention on the droplet clustering within air-assisted sprays. Their measurements were conducted based on the combination of the PIV (Particle Image Velocimetry) technique and the ILIDS (Interferometric Laser Imaging for Droplet Sizing) technique. The result showed that the clustering of droplets occurs over a range of length scales. An experimental investigation of air-assisted spray by Gao et al. [38] showed that the increasing of the ambient temperature led to the deviation in jet trajectory that occurs at the margin of the jet due to the increased vaporization of liquid fuel droplets. In addition, Wu et al. [39] pointed out that the equilibrium position of droplet breakup and coalescence in the air-assisted spray is quite close to the nozzle exit, while the droplet size in the far field is mainly determined by droplet collision.

Currently, the time-resolved characteristics of intermittent air-assisted spray have been rarely concerned. In this study, we focus on the droplet and gas flow behaviors of an air-assisted spray emerging from a pulse-working twin-fluid atomizer. The paper is organized as follows: first, the experimental setup and test conditions are detailed, followed by the outlined data processing method. The main results and discussion including droplet size-velocity statistics, droplet Sauter Mean Diameter (SMD), mass-averaged velocity, local gas flow characteristics and droplet-gas slip velocity will be elaborated in Section 4. This paper closes with a summary and conclusions in Section 5.

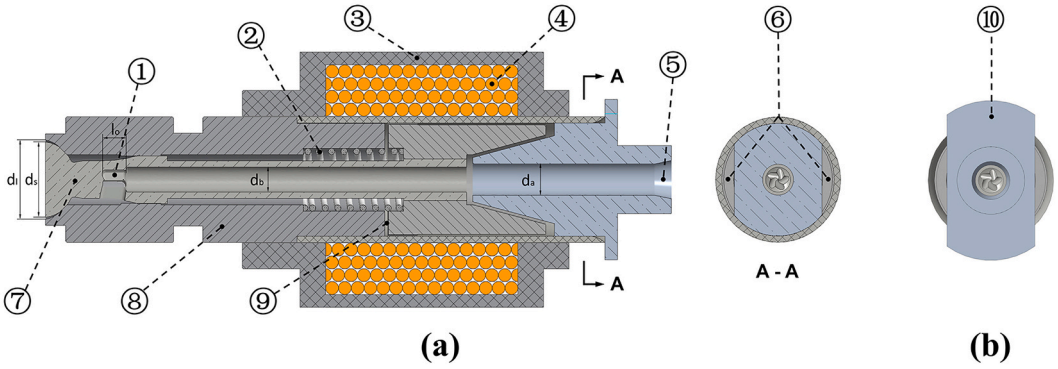

Fig. 1. (a) Section view of the air-assisted injector; (b) side view of fuel and air inlet. Dimensions: $d_a = 3.2$ mm, $d_b = 3.0$ mm, $d_l = 6.6$ mm, $d_s = 6.0$ mm, $l_o = 3.0$ mm. Component name: 1. orifice, 2. spring, 3. coil, 4. yoke, 5. fuel inlet, 6. air inlet, 7. needle plug, 8. shell, 9. working clearance, 10. deflector.

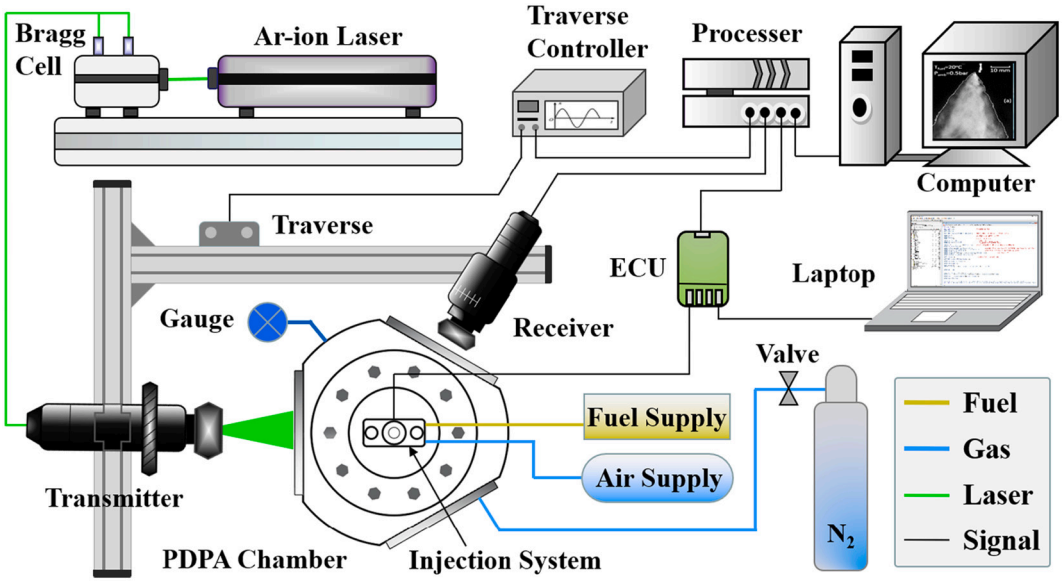

Fig. 2. Schematic diagram of experimental facilities and setup.

2. Experimental setup and test conditions

The operating principle of the air-assisted injection system as well as fluid supply method has been described in sufficient detail in our previous publications [40,41]. A brief summary of air-assisted injector is outlined here for completeness. The internal geometry and dimensions of the air-assisted injector are depicted in Fig. 1. In general, the air-assisted injector is composed of a magnetic yoke, a coil, a shell, a needle plug, a spring, and a deflector. As the principal moving part, the needle plug is designed with a hemispherical head thus an annular diverging flow path between needle plug head and shell is formed. The upstream of the needle plug is made of magnetic material, which will shift by quickly reacting to the electromagnetic force in the magnetic field established by the energized coil. The spring will push the needle plug to return to its primal position after the magnetic field collapses. The working clearance, which determines the maximum displacement of the needle plug and directly dictates the cross-sectional area of the nozzle exit, was maintained at 0.15 mm. Two passages that formed between the middle part of the deflector and the atomizer shell are used for air inlet (see component 6). The liquid fuel is delivered to the injector through the middle hole of the deflector, i.e., component 5. The liquid fuel and air come into contact after passing the deflector and are thoroughly mixed within the hollow chamber (diameter of $d_b = 3.0$ mm) of the needle plug.

The liquid fuel was supplied by an electric fuel pump (12 V and the max. Pressure of 0.9 ± 0.05 MPa), and the air was supplied by a compressed air cylinder (40 L, max. Pressure of 15 ± 0.1 MPa). The compressed air supplied by air cylinder was output with a primary pressure of 0.6 MPa after a relief valve (Seatcio G11-25-1.0). In addition, a combined pair of mechanical differential pressure valves (uncertainty is approximately ±0.005 MPa) was used to precisely stabilize air pressure (referenced to ambient pressure) and fuel pressure (referenced to air pressure) to $P_g = 0.6$ MPa and $P_l = 0.7$ MPa respectively. With the continuous supply of liquid fuel and compressed air, as well as reliable differential pressure valves, constant pressure of liquid fuel and compressed air can be guaranteed and delivered to the atomizer. Please note that the above pressures are all gauge pressures.

The acquisition of spray macroscopic images is carried out based on our high-speed spray visualization test bench. A high-speed (Phantom V7.3) was used to capture transient spray morphology which was illuminated by a backlight of an LED light source. The recording rate was set to 10,000 frames per second (fps) with an exposure time of 2.0 μs and a resolution of 512 × 512 pixels. The corresponding physical image resolution was approximately 0.182 mm/pixel.

A phase Doppler Particle Analyzer from Dantec Dynamics Inc. was used to measure the droplet velocity, droplet size, as well as droplet number flux synchronously. A schematic of the experimental facilities and PDPA setup is shown in Fig. 2. The experimental system mainly

Table 1
Optical parameters of the PDPA system.

Parameter (unit)	Value
Wave length (nm)	514.5
Laser power (W)	0.8
Beam spacing (mm)	37
Bean diameter (mm)	2.2
Transmitter optics (mm)	310
Receiver optics (mm)	500
Scattering angle (°)	70
Frequency shift (MHz)	40
Spatial filter (mm)	0.025
Fringe spacing (μm)	2.226
No. of fringes	21
Spheroidal tolerance	5%

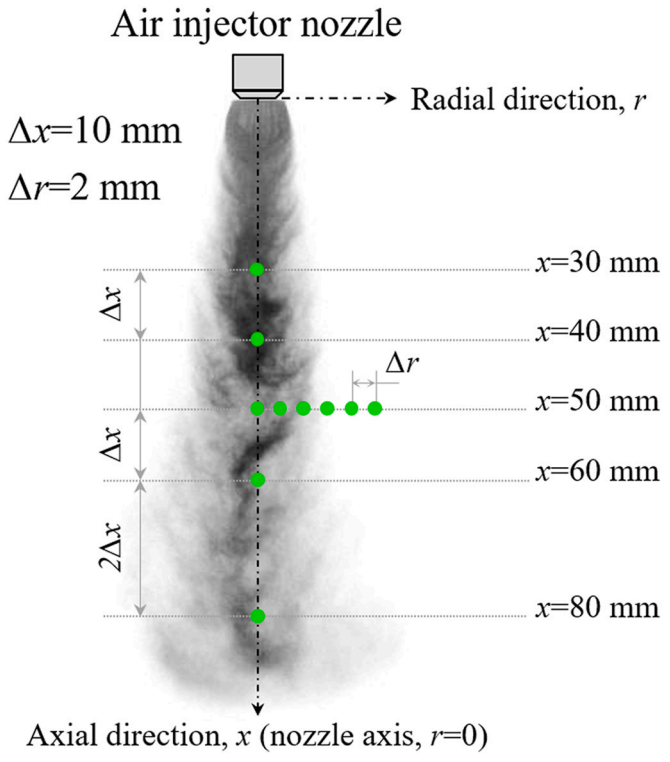

Fig. 3. Details of axial and radial sampling locations superimposed on a spray profile. Note that the dimensions are not to scale.

consists of PDPA, air-assisted injection system, constant volume chamber (CVC), control and data acquisition system (BSA software). The PDPA is a single-point optical measurement method that enables simultaneous measurement of droplet velocity and size. The optical parameters of the PDPA system are listed in Table 1. The laser beam was emitted from an argon-ion laser and then traveled through a Bragg cell to be separated into three pairs of laser beams. The laser of the selected wavelength (514.5 nm) was transferred to the transmitter through an optical fiber and passed through the lens and the quartz window to form an ellipsoidal measurement volume (focus point) inside the CVC [38]. The optical signal receiver was located in the same horizontal plane as the measurement volume and at 110° to the axis of transmitter to effectively capture the first-order scattered signal. The spatial position of measurement volume was adjusted by the traverse system, which enables a minimum displacement of 0.1 mm.

In the PDPA measurements, both subrange and coincidence configurations were set to acquire droplet data. In this case, the subrange configuration set bound for the variables we are examining while the coincidence configuration sorted out all the other data so that only those associated with the data in the subrange remain. The subrange for droplet diameter was set with the maximum value of 45 μm and the subrange for droplet velocity was set to −50 to 200 m/s. No specific subrange of injection time was set since our self-developed electronic control unit (ECU) had been used to output precise trigger signal for both injector and PDPA. The spatial measurement volume positions selected for this study are shown in Fig. 3. To avoid typical sampling failures caused by dense droplets at the nozzle outlet region, the sampling position of the axis started at 30 mm. Since PDPA has a limited droplet capture rate in one single injection for intermittent air-assisted sprays, multiple injections need to be repeated under the same operating conditions.

The control signal sequence for a single injection is shown in Fig. 4. Both the liquid fuel injection drive signal and the air-assisted injector drive signal were employed to configure the drive current with "peak-hold" shape. The peak duration of T_o = 1.5 ms was used to open the nozzle with a quick response, while the hold duration of T_f and T_a was used to keep the nozzle open for fuel injector and air-assisted injector, respectively. T_i represented the injection interval between fuel injector closing and air-assisted opening. The trigger signal of the PDPA was set to synchronize with the air-assisted driving signal. After being triggered, the PDPA operated with a preparatory status and started recording droplet information when droplets flowed through the measurement volume. However, after the air-assisted injector was opened, the spray generally took some time (T_{arrive}) to reach the measurement volume. The sampling cycle was automatically set by the PDPA's acquisition system, which divided the time after the trigger into a series of time bins according to a fixed duration (denoted by ΔT_{bin}) and numbered them sequentially. Based on the droplet information obtained within these time bins, a time-resolved microscopic characteristic comparison can be performed.

In order to avoid interference between droplets generated from different injections, the frequency of the repetitious injection was set no more than 1 Hz (i.e., the injection cycle time is greater than 1 s, which is much longer than the nozzle opening duration). In addition, a nitrogen cylinder is connected to the CVC through a valve and is used to sweep out the exhaust gas and the fuel mist of each measurement. The ambient pressure and temperature inside the constant volume chamber were 0.1 MPa and 20 °C, respectively. The corresponding air density and dynamic viscosity were $\rho_g = 1.205$ kg/m^3 and $\mu_g = 0.018 \times 10^{-3}$ kg/(m • s). The liquid fuel used in the experiments was n-octane (C_8H_{18}). The liquid density, viscosity and surface tension were $\rho_l = 748$ kg/m^3, $\mu_l = 1.36 \times 10^{-3}$ kg/(m • s) and $\sigma = 0.0255$ kg/s^2. All physical properties were obtained at room temperature and the local barometric pressure.

The control parameters in this study include T_a (ranges from 0.5 ms to 3.0 ms) and T_i (ranges from −0.5 ms to 2.0 ms) under a constant T_f. The measuring volume was set to cover various radial r as well as axial x positions. The main spray characteristics parameters of interest include the droplet diameter and velocity joint probability density distribution function (JPDF), the Sauter Mean Diameter of sampled droplets, droplet mass-averaged velocity U_m, local gas velocity and turbulence intensity, and the droplet-gas mean slip velocity U_{slip}.

3. Data processing and uncertainty

3.1. Sensitivity of time bin size

PDPA records the diameter, velocity, as well as the arrival time of spray droplets when they pass through the measurement volume. In this study, we divided the captured droplets into multiple time bins and number them in sequence based on droplet arrival time. The average droplet velocity and diameter were calculated from the sampled droplets within each individual time bin. Therefore, the numbering of the time bins (denoted by Bin No.) essentially referred to the concept of time. It should be noted that the time bin size was a compromise between the number of sampled droplets and the time resolution. To characterize the

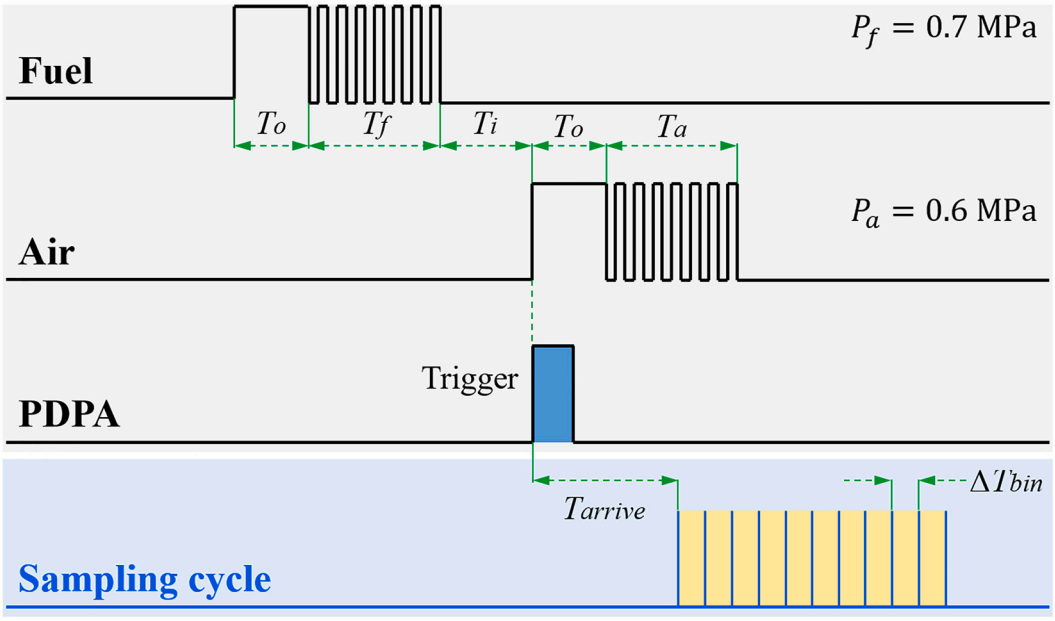

Fig. 4. The drive signal output by ECU (gray background) and the sampling cycle set by BSA for intermittent spray (blue background). (For interpretation of the references to color in this figure legend, the reader is referred to the web version of this article.)

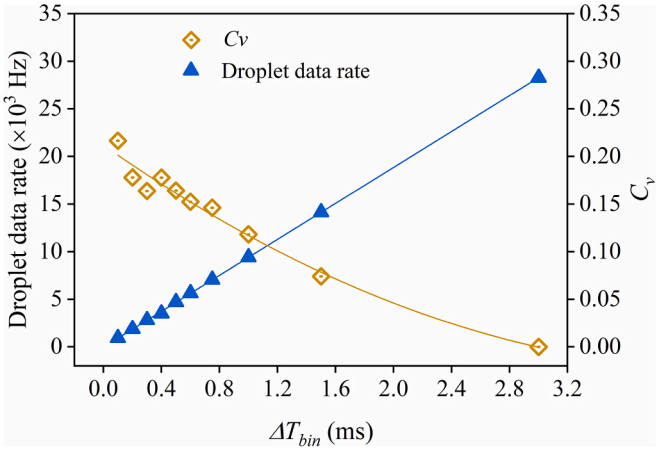

Fig. 5. Sensitivity performance of droplet sampling data as a function of temporal resolution ΔT_{bin} at x = 30 mm, r = 0 mm.

sensitivity of time bin size, we first extracted the sampling time of 3.0 ms (including 2.5 ms when the nozzle was open and 0.5 ms after the nozzle was closed) from the moment when spray reached PDPA measurement volume as the raw droplet sampling data. The raw droplet sampling data was subsequently grouped into different time bins according to the bin size and the droplet arriving time when it was recorded. Then, the average spray droplet data within these bins and the coefficients of variation (denoted by C_v) were calculated.

Fig. 5 shows the sensitivity performance of droplet sampling data as a function of temporal resolution ΔT_{bin} at x = 30 mm, r = 0 mm. A significant linear increasing correlation was found between spray droplet data and ΔT_{bin}, which implies that the droplets were uniformly distributed in terms of sampling time. This observation indicates that the droplet data decreases with the increase of temporal resolution. In addition, a quadratic polynomial function can be used to fit the C_v of droplet data versus ΔT_{bin}. Therefore, a compromise of time bin size of ΔT_{bin} = 0.5 ms was employed in this study for sampling time division and subsequent analyses on account of sufficient droplet data and

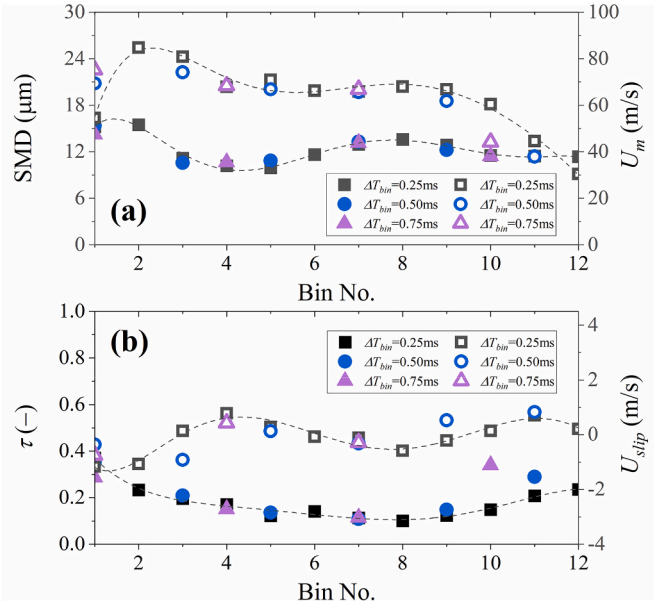

Fig. 6. Effect of time bin size (ΔT_{bin}) on spray characteristics: (a) SMD and mass-averaged velocity, (b) gas-phase turbulence intensity and droplet-gas mean slip velocity at x = 30 mm, r = 0 mm. Note that the time bins are numbered with respect to the smallest bin size of ΔT_{bin} = 0.25 ms.

reasonable coefficient of data variation.

In addition, we further evaluated the effects of ΔT_{bin} on the time-resolved spray characteristics. Here, three sets of time bin size, i.e., ΔT_{bin}=0.25 ms, 0.50 ms, and 0.75 ms, were adopted for comparison, as seen in Fig. 6. It should be noted that the time bins were numbered with respect to the smallest bin size of ΔT_{bin}=0.25 ms. The time-resolved droplet SMD and mass-averaged velocity are shown in Fig. 6(a). No significant variation was observed for various ΔT_{bin} cases, and the same result also held true for the effect of ΔT_{bin} on time-resolved gas-phase turbulence intensity and droplet-gas mean slip velocity, as presented in Fig. 6(b). An apparent fact is that the sampled droplet data within each

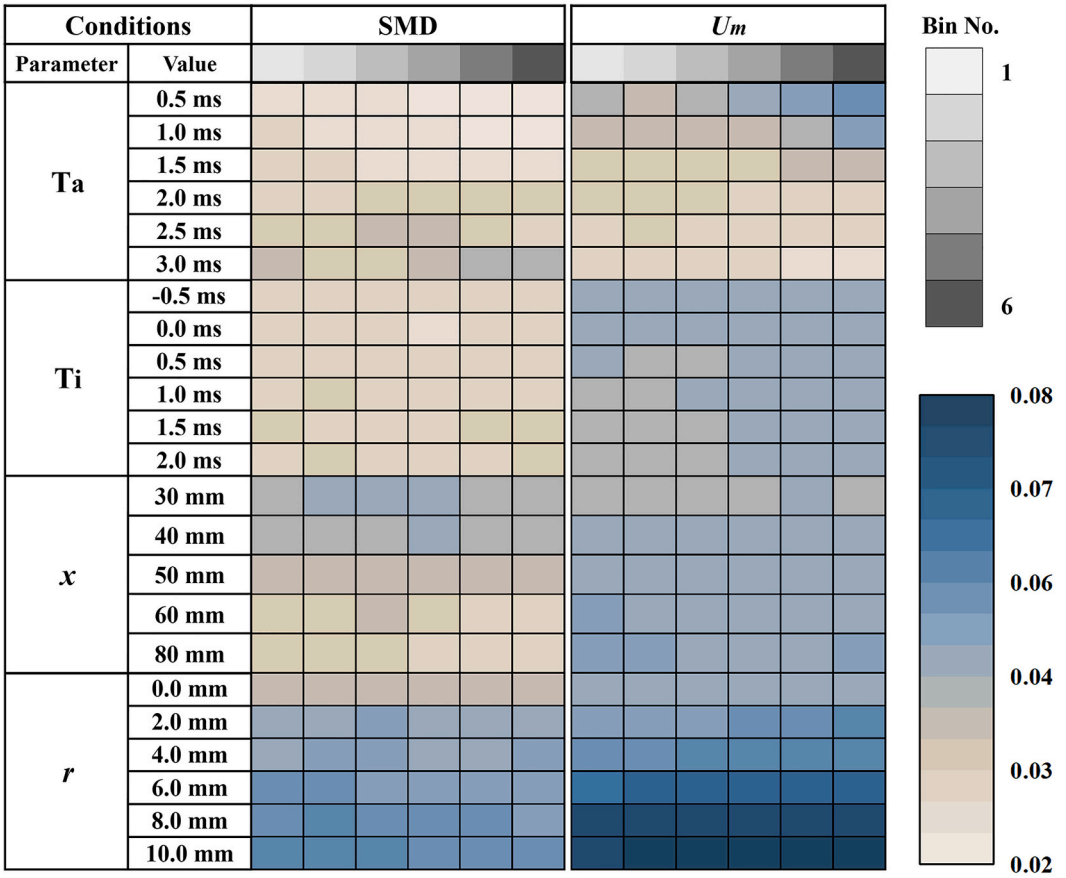

Fig. 7. Performance of measurement uncertainties under different operating conditions.

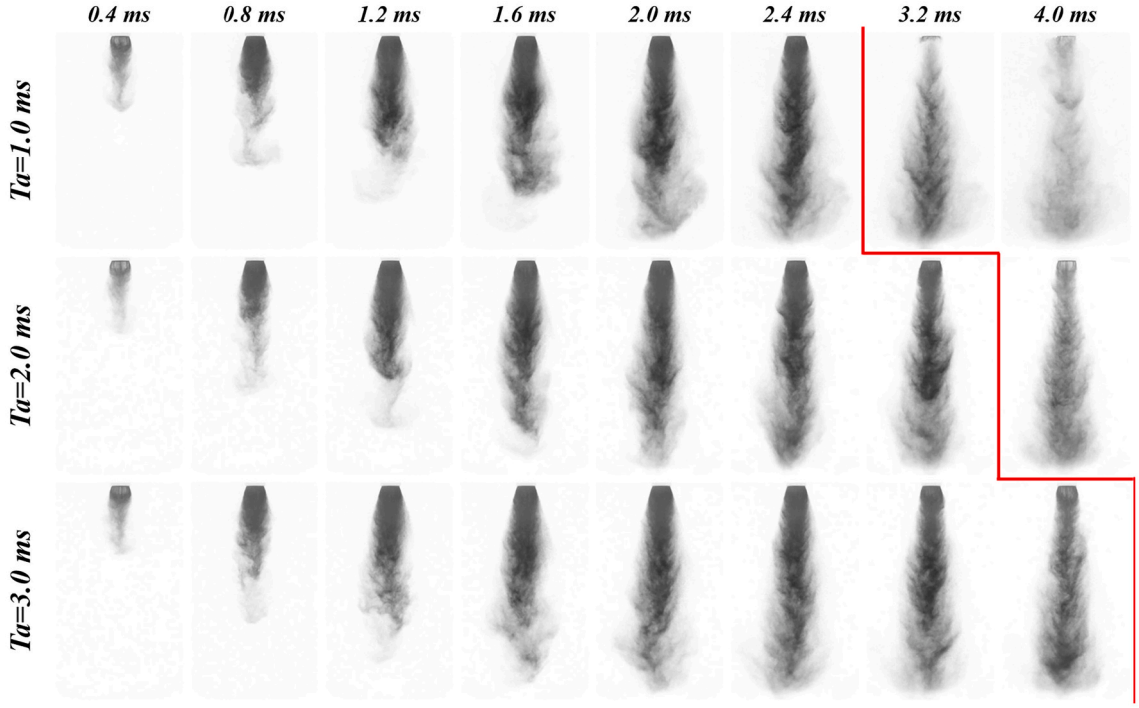

Fig. 8. Spray images under various air injection durations. The raw image has been processed by background removing and conversion from RGB to grayscale.

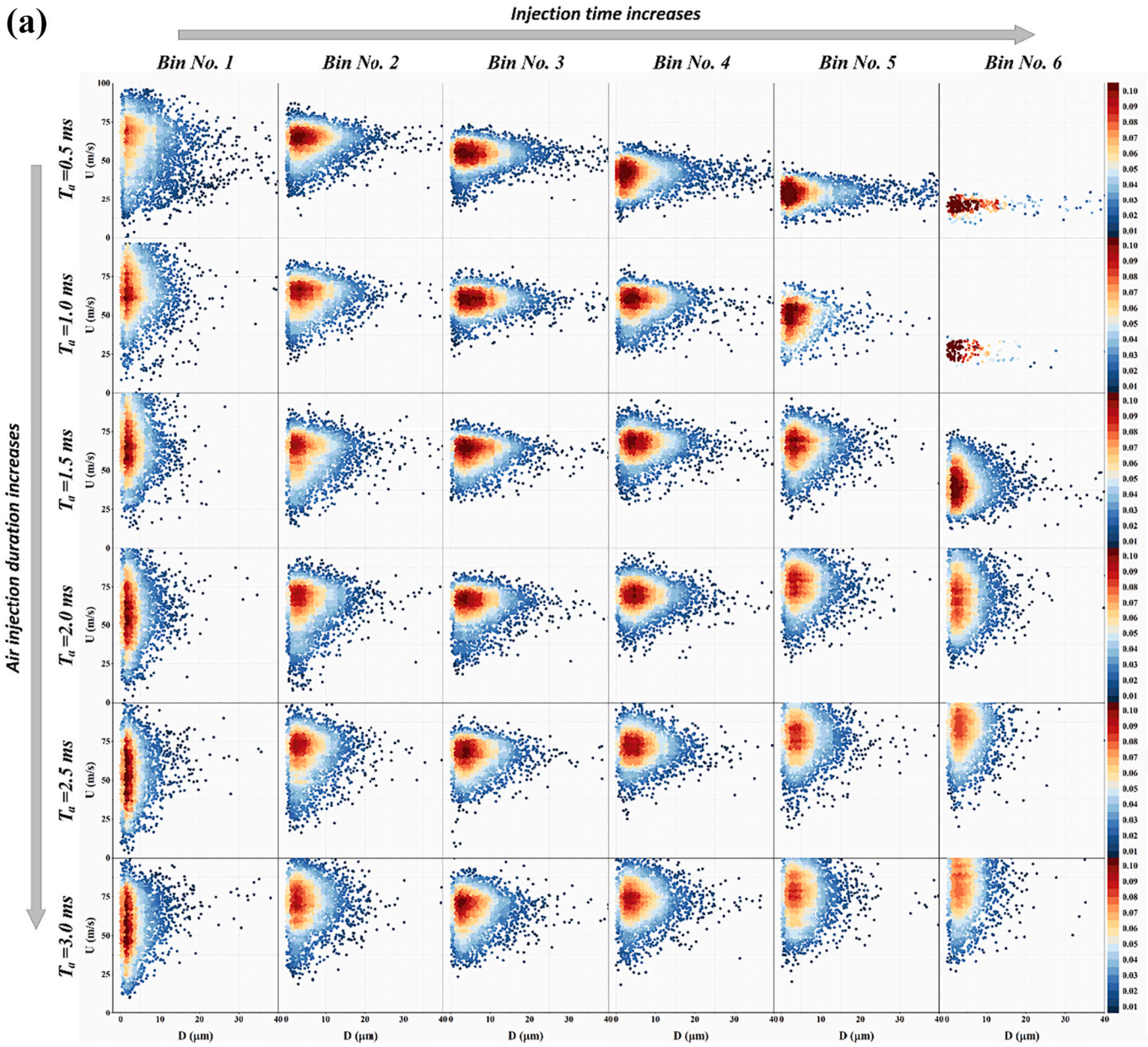

Fig. 9. Droplet size-velocity correlation and distribution colored by JPDFs under (a) various air injection durations, (b) various fuel-air injection intervals, (c) various axial sampling positions and (d) various radial sampling positions.

time bin decreases as the bin size decreases. However, it can be concluded that the influence of the sampling time bin division on the spray and droplet characteristics can be neglected for the intermittent air-assisted spray in this study.

3.2. Uncertainty analysis

The droplet sampling data rate for the same working condition was not less than 10,000 Hz. The method of estimating the measurement uncertainty (E_x) has been specified in our previous publication [35], as

$$E_x = \pm \frac{S_E}{\bar{x}}, \text{where } S_E = \sqrt{\frac{\sum_{i=1}^{N}(x_i - \bar{x})^2}{N(N-1)}} \quad (1)$$

here S_E is the standard error of sampled droplet data. $\bar{x}$ denotes the arithmetic mean of droplet data with a sample space of N. Note that the E_x represents the normalized result of standard error and $\bar{x}$ from experimental measurement data. A Matlab colormap [42] was employed to represent comprehensive data performance of uncertainty values, as shown in Fig. 7.

One can see that the variation in the uncertainty of SMD measurements at different air injection durations and fuel-air injection intervals is not particularly noticeable. A slight bin-to-bin variation can be observed under different T_a cases, however, absent for different T_i cases which indicates the relatively limited influences of T_i on the spray characteristics. In addition, the spatial sampling position shows a greater impact on the measurement uncertainties than the injection control parameters. The uncertainty values of radial sampling positions are generally larger than these values of axial sampling positions, which is attributed to the reduction of the radial sampling data as r increases. The uncertainty of droplet mean velocity is relatively large and shows an increasing function of r due to the drastic decrease of sampled droplet

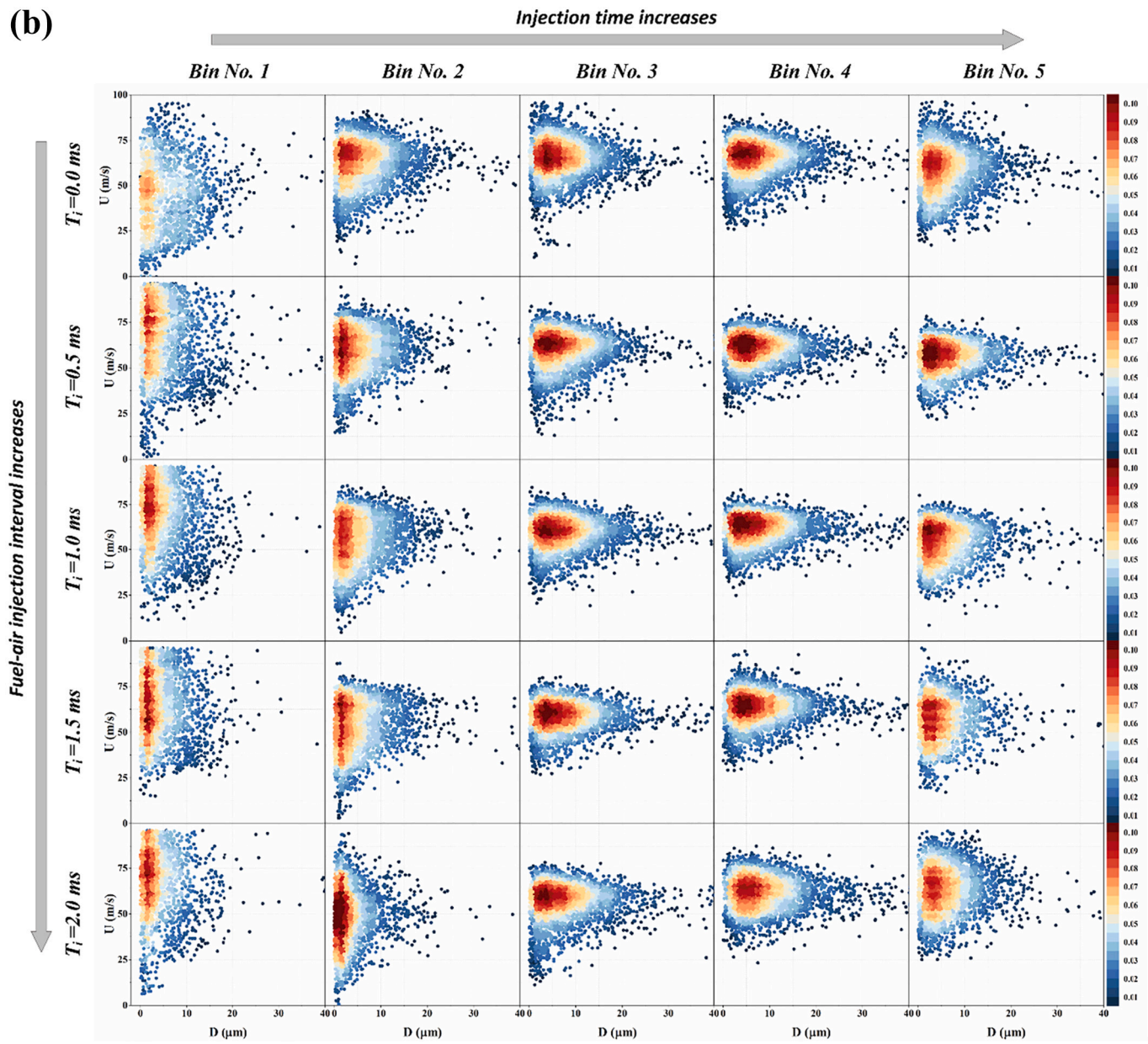

Fig. 9. (*continued*).

velocity away from the spray axis. Overall, none of the measurement uncertainties has exceeded 8%, which implies a relatively acceptable range of experimental tolerances.

4. Results and discussion

4.1. Spray images

Fig. 8 shows the spray image sequence obtained from selected frames after the start of trigger (ASOT). Since the fuel-air injection interval shows no significant effect on the spray morphology according to our previous study [41], only the spray images under different air injection durations (T_a = 1.0 ms, 2.0 ms and 3.0 ms) are examined here for comparison. The red line in the figure is used to distinguish the injector status as opening (left side) and closing (right-side). When the injector is open, no significant variation in time-resolved spray morphology between different air injection durations can be observed. In addition, one can see that the spray color of T_a = 1.0 ms has become progressively lighter after 3.2 ms ASOT. The same phenomenon is found at around 4.0 ms ASOT for T_a = 2.0 ms and is absent for T_a = 3.0 ms. This observation can be explained by the fact that the air injection duration determines the duration of the injection process. When T_a is 1.0 ms, the injection process lasts approximately $T_a + T_o$ = 2.5 ms, which increases to 3.5 ms and 4.5 ms for the case of T_a = 2.0 ms and T_a = 3.0 ms.

4.2. Droplet size-velocity JPDFs

Droplet size and velocity distribution are important parameters to visualize the data range and dispersibility characteristics of the spray droplets [42]. Unlike previous studies where the droplet diameter and velocity distributions were calculated separately, this study adopts the droplet size-velocity joint probability density function to demonstrate the combined microscopic information of droplets [43]. As the droplets pass through the PDPA measurement volume, the droplet velocity U and diameter D, as well as the transit time t are accurately recorded. Given that the droplet with the droplet diameter distribution in the range of [D

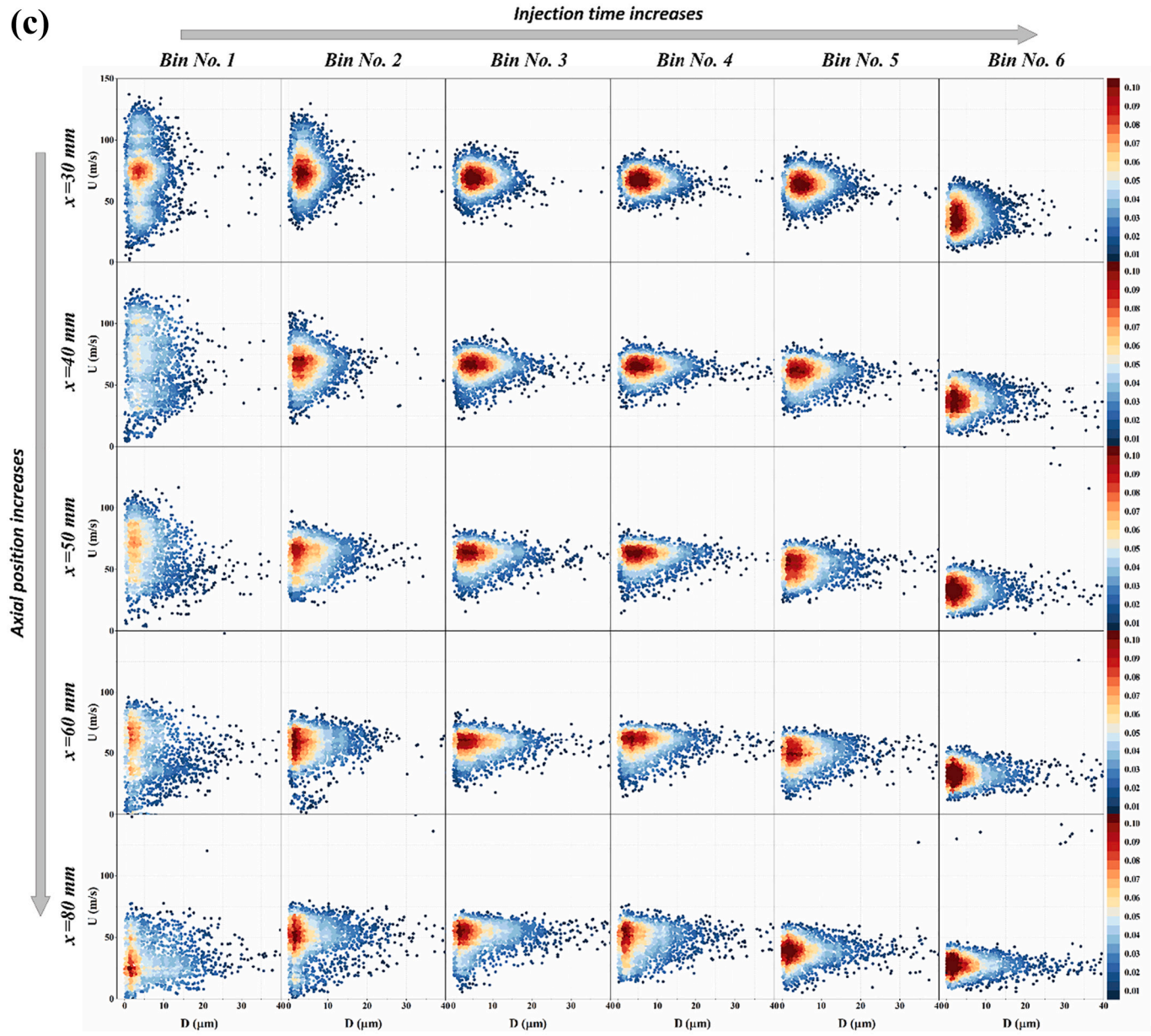

Fig. 9. (*continued*).

$- dD, D + dD]$ and the velocity distribution in the range of $[U - dU, U + dU]$, the joint probability density function represents the probability that the droplet diameter distribution is in the range of dD and the droplet velocity distribution is in the range of dU, yields

$$\int (U, D) dU dD = P(U \cap D) \tag{2}$$

In this study, the value of $dD = 1.0$ μm and $dU = 2.0$ m/s were employed for the discretization of the sample data. The procedure to obtain JPDF is typified as follows. Firstly, the droplet velocity distribution and diameter distribution based on transit time are attained. Then the distribution of droplet velocity versus diameter can be obtained by taking transit time as a bridge. Finally, the droplets are divided and colored according to their corresponding JPDF value to obtain the probability density distribution diagram that visualizes the joint droplet size and velocity.

The plots of droplet size-velocity distribution colored by JPDFs for partial T_a cases as a function of Bin No. (numbers of sampling time bin divided by $\Delta T_{bin} = 0.5$ ms) are shown in Fig. 9(a). The results are reported for the Bin No. up to 6, and the measurement volume location of $x = 50$ mm, $r = 0$ mm. The following trends can be observed.

(a) The droplet diameter range is generally independent of T_a and Bin No. since all sampling droplets are found to be distributed in the range of 0–40 μm. Most of the measured droplet velocities are less than 100 m/s and a notable time dependent droplet velocity distribution can be observed for all T_a cases.
(b) Droplets are principally concentrated in the diameter range of 0–10 μm with a maximum JPDF close to 0.1. However, the droplet velocity corresponding to the maximum value of JPDF is not constant due to the variation of the droplet velocity range. A significant unimodal distribution of droplet size-velocity JPDFs is found for all cases of T_a and Bin No. A visually identifiable Log-normal distribution of droplet size and a Gaussian distribution of droplet velocity can be inferred, which is consistent with our previous results for droplet distribution statistics [39,40].
(c) For $T_a = 0.5$ ms and $T_a = 1.0$ ms, the number of captured droplets with Bin No. 6 is remarkably low due to the early closure of the

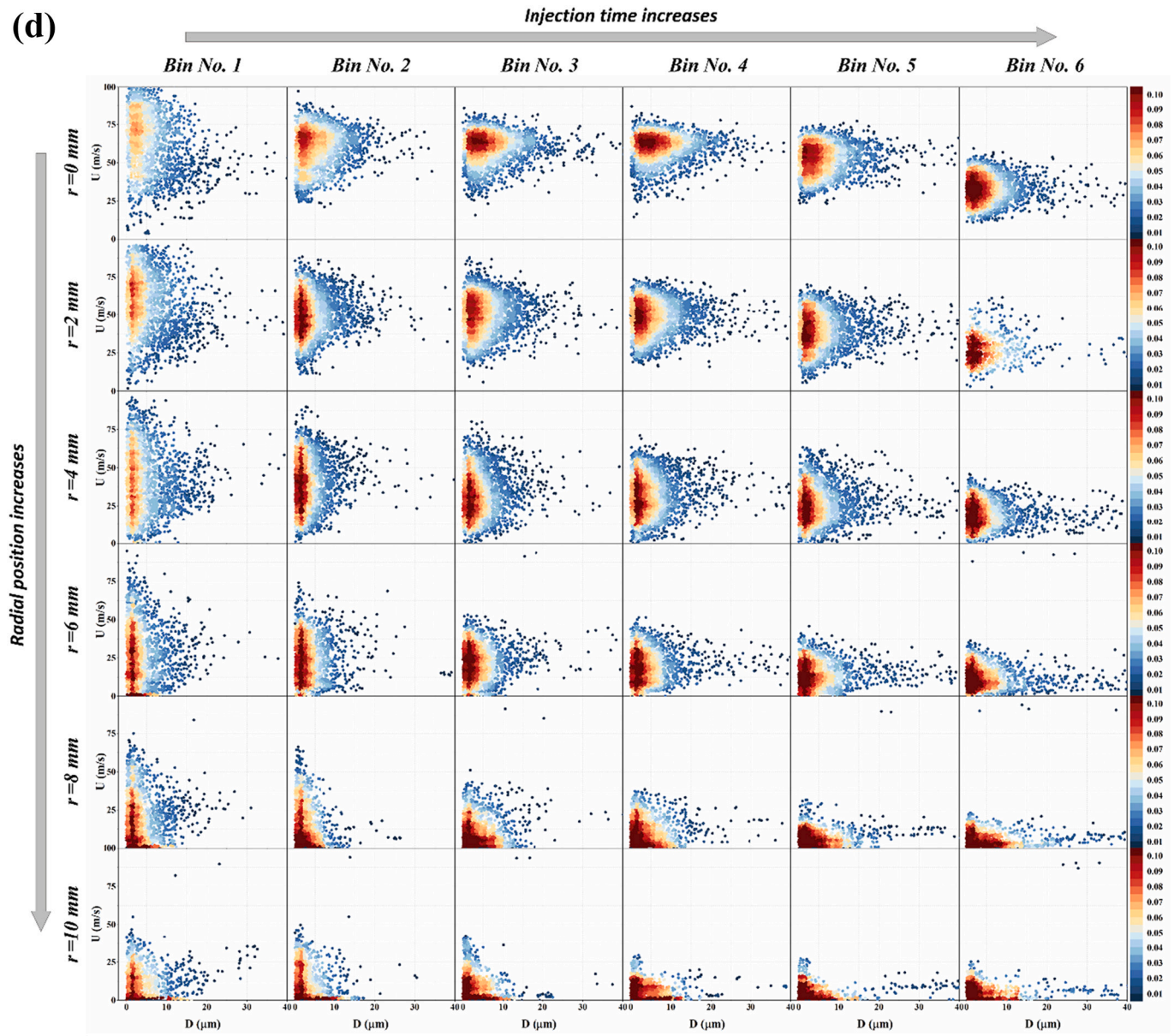

Fig. 9. (*continued*).

air-assisted injector, which is absent for other cases with the increase of T_a. When T_a exceeds 1.5 ms, it is interesting to note that the temporal droplet velocity range first decreases (Bin No. 1–3) and then increases (Bin No. 4–6). The velocity of some droplets even exceeded 100 m/s. This is because the continuously injected air in the later stage of spray keeps accelerating the droplets at the spray tail since a large amount of liquid fuel is concentrated in the spray head and has been already sprayed.

The time-resolved droplet size-velocity correlation and distribution colored by JPDFs under various fuel-air injection intervals, various axial and radial positions can be found in Fig. 9(b)–(d). No distinguishable difference of both droplet diameter and velocity range as well as the presentation of JPDF as a function of T_i and Bin No. can be seen. This implies that fuel-air injection interval has a negligible effect on air-assisted spray within a selected parameter range. In the spray centerline, the droplet velocity range shows a noticeable decrease with axial position for all Bin No. This trend also applies to the cases when radial sampling position moves away from spray axis toward the outer region. At $r = 10$ mm, the droplets are found concentrated in the lower left corner of each U—D plot, which indicates that droplets sampled at the radial edge of the spray possess a moderate size and low velocity.

4.3. Droplet sampling rate

Droplet data rates of different time Bin No. during PDPA measurements were calculated to characterize the time-resolved variation. Here, normalized data rate was used to represents the ratio of the number of sampled droplets during some selected time Bin No. to the total number of droplets captured during all time bins. Fig. 10 shows the normalized droplet data rate as a function of Bin No. under various air injection durations. For $T_a = 0.5$ ms and $T_a = 1.0$ ms, The sampling rate first remains constant and rapidly decreases in the late spraying period. This is attributed to the closing of the injector and the termination of the spray caused by a relatively short injection duration. Contrastively, a relatively consistent sampling rate of 0.16 under different Bin No. can be seen when $T_a \geq 1.0$ ms, which indicates that a relatively well-balanced and stable droplet data sampling can be attained within the opening

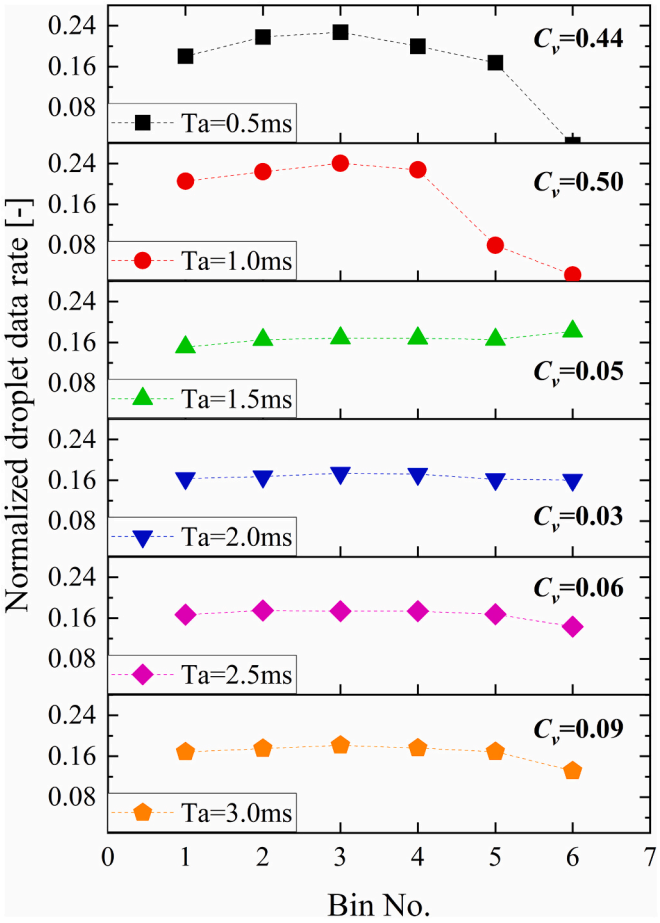

Fig. 10. Normalized droplet data rate captured by PDPA under various air injection durations.

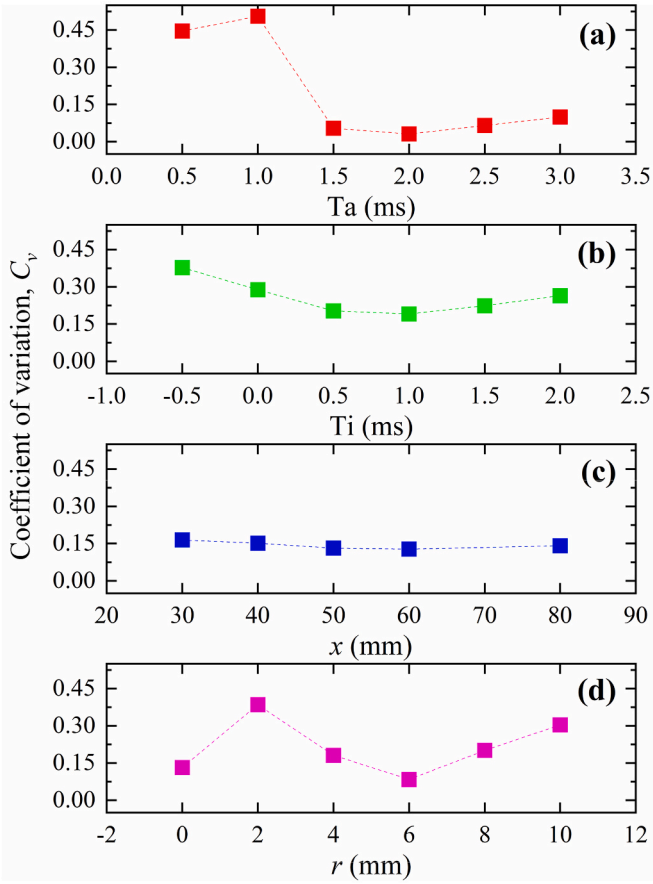

Fig. 11. Coefficient of variation of droplet sampling data rate under different control parameters.

duration of air-assisted injector.

The estimation of variation is quantified by the coefficient of variation (denoted by C_v), which represents the ratio of the standard deviation σ_x to the arithmetic mean of the data rate $\bar{x}$, as $C_v = \sigma_x/\bar{x}$. The C_v for the cases of $T_a = 0.5$ ms and $T_a = 1.0$ ms has exceeded 0.4, which is an order of magnitude larger than other cases, see Fig. 11(a). This is somewhat expected since the early closure of the air-assisted injector caused a relatively short injection duration and significant variations in sampled droplet data for different Bin No. Fig. 11(b-d) shows the coefficient of variation under other control parameters. A moderate variation can be found when T_i increases from −5 ms to 2.0 ms. The pronounced difference in C_v at $T_i = -0.5$ ms and $T_i = 0.0$ ms is most likely attributable to the special fuel-air mixing status upstream air-assisted injector since the air-assisted injector opens when the liquid nozzle has not been fully closed. A nearly constant C_v can be observed for different axial sampling positions, which implies that, along the spray centerline, the time-resolved droplet sampling process is relatively stable. However, the time-resolved C_v of droplet sampling data rate varies over a wide range as the sampling position moves away from the spray axis. Therefore, it can be inferred that there may be considerable inconsistency in the air-assisted spray evolution and spatial distribution of droplets at different spray radial positions.

4.4. Sauter Mean Diameter

The average diameter of the sampled droplets is characterized by Sauter Mean Diameter (SMD), which is calculated by

$$\mathrm{SMD} = \sum D_i^3 \Big/ \sum D_i^2 \tag{3}$$

here D_i is the diameter of the ith sampled droplet. The droplet SMD was calculated for different sampling Bin No. under different operating conditions, as shown in Fig. 12. Note that only three sets of control parameters are selected here to demonstrate and compare data trends in each subgraph.

A positive correlation between droplet SMD and air injection duration can be observed in Fig. 12(a), which indicates that the increase in air injection quantity promotes spray atomization. For $T_a = 0.5$ ms, an incremental trend of SMD over time can be seen. Due to the termination of atomization energy input caused by nozzle closure, the limited aerodynamic forces cannot further promote droplet breakup while collision and coalescence between discrete droplets will dominate the subsequent droplet size. In contrast, fuel-air injection interval shows an insignificant impact on droplet SMD, as seen in Fig. 12(b), which proves that fuel-air injection interval does not affect the spray atomization quality. Along the spray axis, no variation of droplet SMD under different Bin No. can be found. However, the SMD shows an increasing function of axial position from nozzle exit. This can be attributed to coalescence of colliding droplets as they travel downward [39]. As the sampling position moves radially from the spray axis to the spray edge, a moderate trend of SMD reduction can be identified. In addition, the SMD of different radial positions increases with time and the variation of SMD between different radial positions tends to be less pronounced.

4.5. Droplet mass-averaged velocity

The air-assisted spray is characterized by frequent gas-liquid mo-

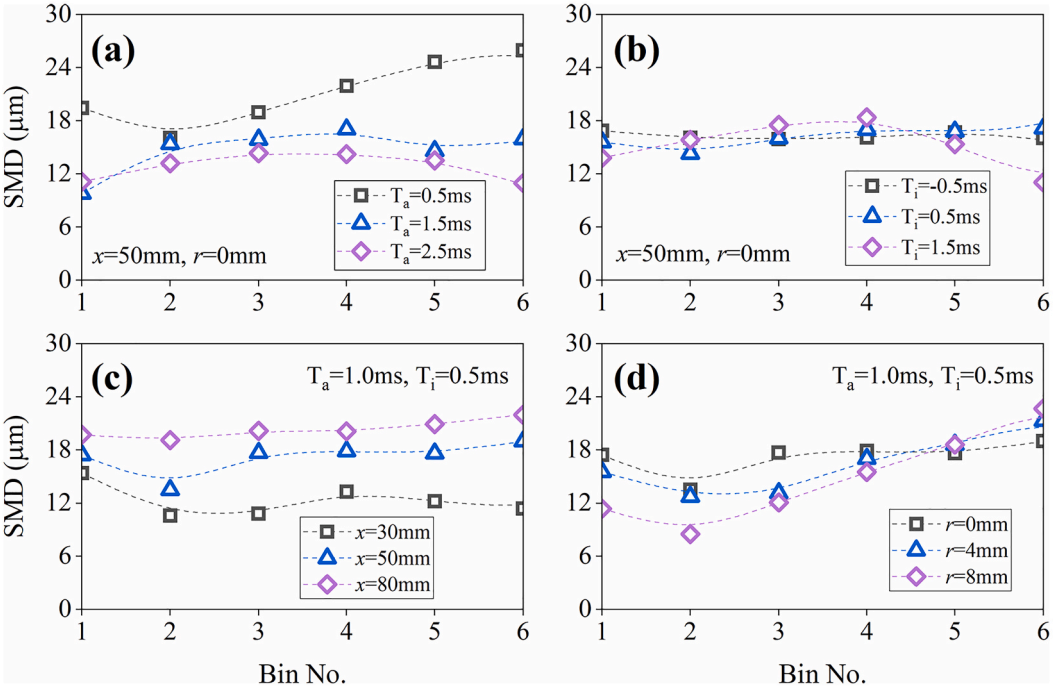

Fig. 12. Time-resolved droplet Sauter Mean Diameter under (a) various air injection durations, (b) various fuel-air injection intervals, (c) various axial positions, and (d) various radial positions.

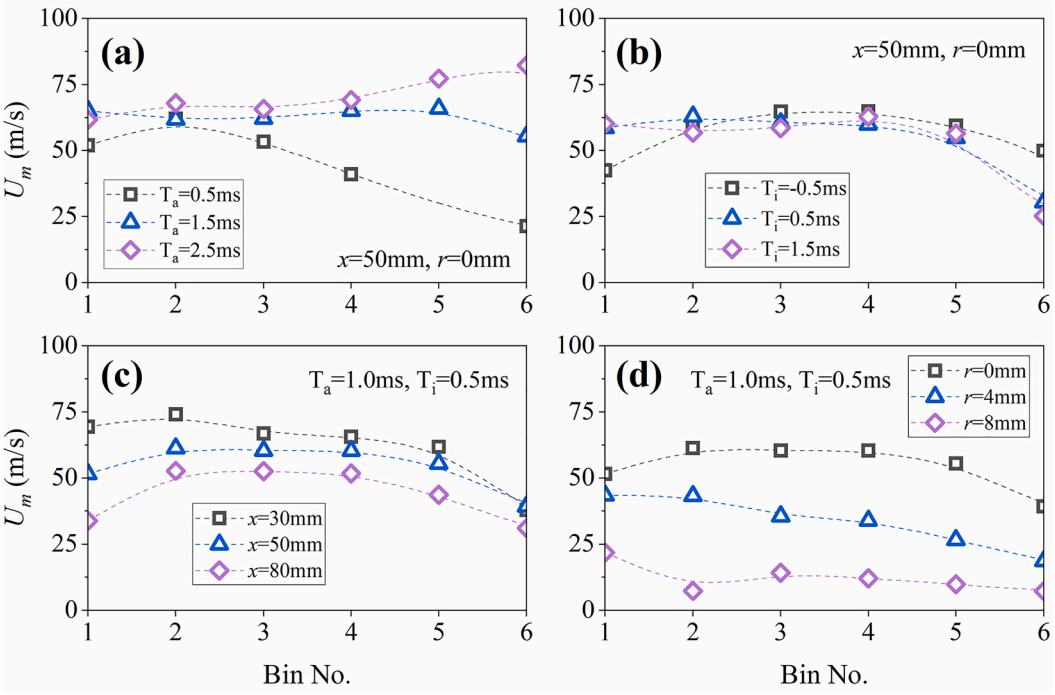

Fig. 13. Time-resolved droplet mass-averaged velocity under (a) various air injection durations, (b) various fuel-air injection intervals, (c) various axial positions, and (d) various radial positions.

mentum transfer within the spray field [13,44]. The energy used to atomize liquids in this air-assisted spray comes primarily from the gas jet and interphase energy transfer from gas phase to liquid phase. In this study, droplet mass-averaged velocity U_m was used to characterize the mean velocity of sampled droplets [34], as

$$U_m = \frac{\sum D_i^3 U_i}{\sum D_i^3} \tag{4}$$

where U_i is the velocity of the ith sampled droplet. The above calculation is based on the principle that the sum of all sampled droplet momentum is constant, i.e. the actual sum of momentum of all sampled droplets is

Table 2
Properties of tracer droplets with a diameter of 5 μm under various air injection durations.

Condition	U_T (m/s)	τ_0 (ms)	*Stk* (−)
T_a = 0.5 ms	0.293	0.043	0.080
T_a = 3.0 ms	0.293	0.043	0.107

equal to the sum of droplet momentum calculated assuming that all droplet velocities are the droplet mass-averaged velocity. The mass-averaged velocities under different conditions are shown in Fig. 13.

Fig. 13(a) shows that the effect of air injection duration on the time-resolved droplet mass-averaged velocity is primarily manifested in the late sampling period (Bin No. 4–6). At T_a = 0.5 ms, the droplets gradually lose the energy supplied by the gas jet at Bin No. 4–6 due to the closing of the nozzle. Fig. 13(b) shows that the fuel-air injection interval still has no significant influence on the droplet mass-averaged velocity. The mass-averaged velocity of the droplets decreases as the sampling position moves in both the axial and the radial direction, see Fig. 13(c-d). This indicates that the high velocity droplets appear in the spray field near the axis as well as in the region of the nozzle exit. Due to the dragging force of the surrounding stationary air, it can be seen that the droplet decelerates more rapidly in the radial direction compared to the axial direction. In light of sampling time, it can be found that the droplet mass-averaged velocity at all selected locations tends to decrease after maintaining a relatively stable value.

4.6. Local gas velocity decay

In the study of gas-liquid two-phase spray, discrete droplets are dispersed in the gas stream. The velocity characteristics of the gas phase are essential for further understanding of the droplet-gas interactions and droplet breakup analysis [7]. However, it is admittedly difficult to make simultaneous measurements of the carrier phase velocity while accurately measuring the dispersed phase under experimental conditions [45]. For the application of planar optical diagnostics (mostly Particle Image Velocimetry, PIV) technique to measure gas velocity, a sufficient number of small particles (normally less than 5 μm) have to be used to seed the gas phase [22]. This technique is recommended for the cases where there is pronounced discrimination in size between droplets and seed particles, which is not applicable to our study because the droplet size in our spray is generally small according to above results. Therefore, we adopted PDPA to simultaneously measure widely distributed droplet sizes and velocities, and to further determine the gas phase flow by treating relatively smaller droplets as tracer particles for its simplicity and convenience.

In this study, sufficiently smaller droplets (<5 μm) are distinguished to use them to characterize the local gas phase flow velocity since the followability of 5 μm droplet for gas flow has been well recognized and this concept has been adopted extensively in previous studies [40,46,47]. Therefore, the gas velocity can be calculated by

$$U_g = \overline{U_t} \tag{5}$$

where U_t denotes the velocity of tracer droplet. The terminal velocity, relaxation time, and Stokes number of tracer droplet with diameter D can be calculated respectively by [39,48]

$$U_T = \sqrt{\frac{4gD}{3C_d}\left(\frac{\rho_l - \rho_g}{\rho_g}\right)} \tag{6}$$

$$\tau_0 = \frac{\rho_l D^2}{18\mu_g} \tag{7}$$

$$Stk = \frac{\tau_0}{\tau_t} \tag{8}$$

here C_d is the drag coefficient. τ_t represents the characteristic time of the flow. Due to the prominent turbulent characteristics of the high-speed jet, the characteristic time τ_t can be generally characterized by introducing a turbulent time scale, as $\tau_t = L/u_r$, where L is the turbulence length scale and u_r is the standard deviation of carrier phase fluctuating velocity $\sqrt{\langle U_g U_g \rangle}$ [46]. The study of Longmire and Eaton [49] indicated that the local particle dispersion seems to be governed mainly by the

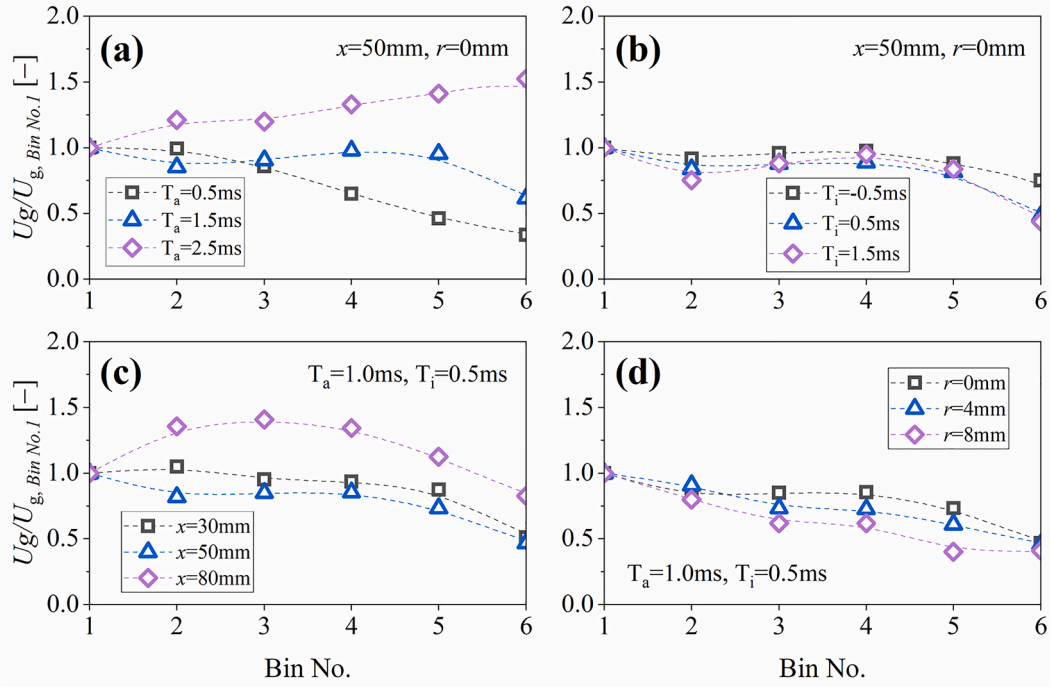

Fig. 14. Time-resolved normalized local gas flow velocity under (a) various air injection durations, (b) various fuel-air injection intervals, (c) various axial positions, and (d) various radial positions.

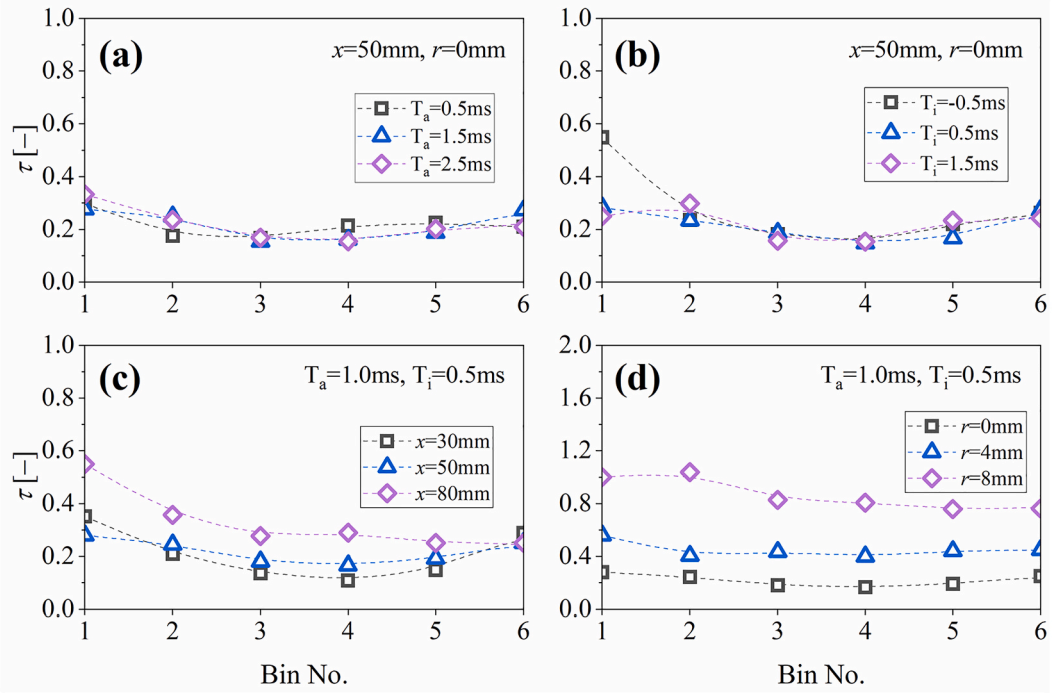

Fig. 15. Time-resolved local turbulence intensity of gas phase under (a) various air injection durations, (b) various fuel-air injection intervals, (c) various axial positions, and (d) various radial positions.

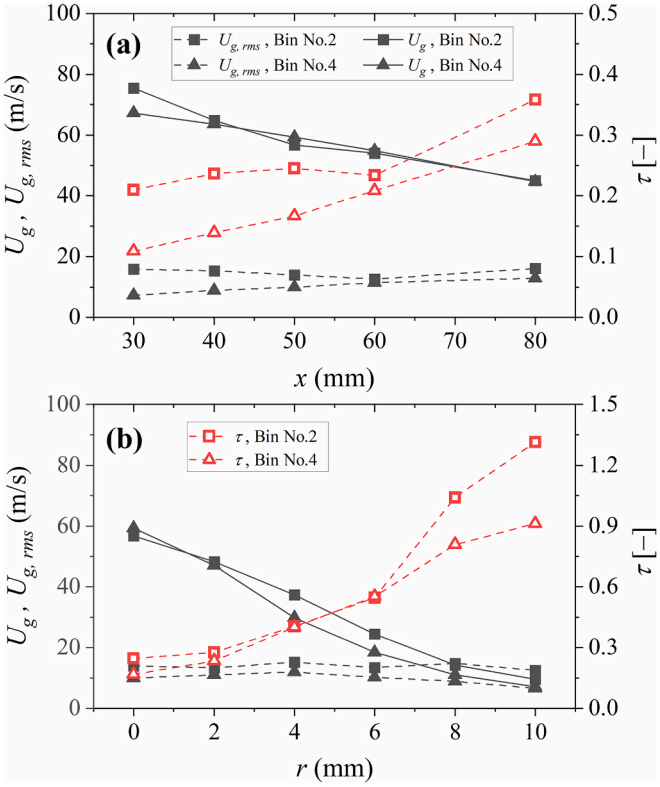

Fig. 16. Mean flow, r.m.s. of fluctuating velocity, and turbulence intensity of gas phase under (a) various axial positions and (d) various radial positions for Bin No. 2 and Bin No. 4.

large-scale turbulent structures of the gas phase. Subsequently, the half width of jet/spray (denoted by $L_{1/2}$) has been widely used to characterize the large turbulence scale, as seen in the Ref [37, 39, 40, 46, 50].

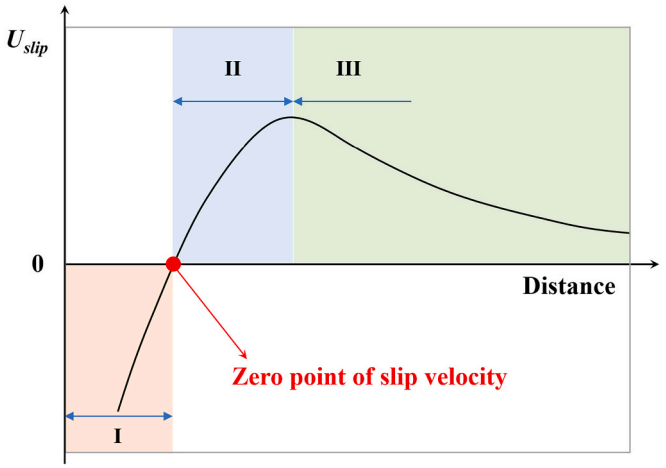

Fig. 17. Downstream evolution of droplet-gas mean slip velocity. Region I: droplet accelerated by gas flow; Region II: droplet velocity overshooting; Region III: droplet decelerated by drag force from surrounding gas flow [44].

Manish and his co-workers [37] proposed that the $L_{1/2}$ can be quantified by the radial location measured from the spray axis where the droplet mean velocity is half of the mean velocity at the spray center. Therefore, the same method was adopted to obtain $L_{1/2}$ in the present study.

The above parameters are evaluated under different conditions for selected tracer droplets with the diameter of 5 μm, see Table 2. It can be seen that the terminal velocity and relaxation time of the largest tracer particle are relatively small, impling favorable ability in air suspension. Since $Stk \ll 1$, the followability of 5 μm droplet is thus justified.

Fig. 14 shows the local gas flow velocity which is normalized by the value of Bin No. 1, as $U_g/U_{g,\ Bin\ No.\ 1}$ to demonstrate time-resolved trend of gas flow velocity. The temporal decay of the gas flow velocity shows different trends at different air injection durations. In which, the termination of the jet caused by the nozzle closure leads to a rapid decay

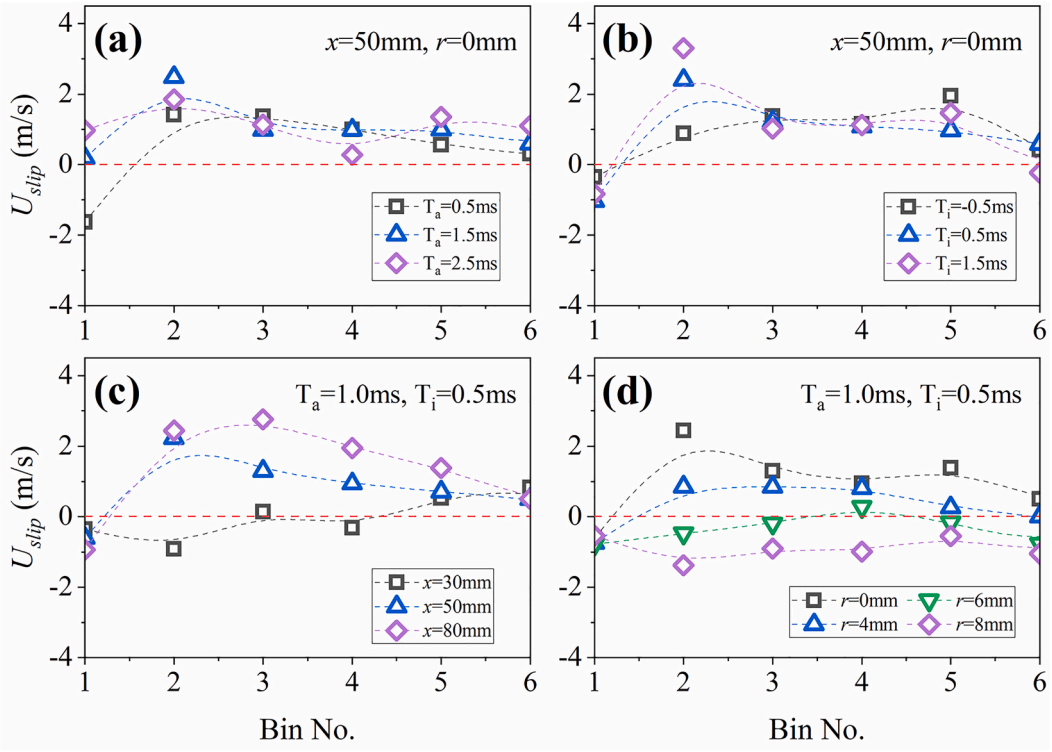

Fig. 18. Time-resolved droplet-gas mean slip velocity under (a) various air injection durations, (b) various fuel-air injection intervals, (c) various axial positions, and (d) various radial positions.

of the gas velocity in the spray field with time. In contrast, when the air injection duration is gradually increased to 2.5 ms and above, the gas velocity can be found to increase instead. This suggests that since a large portion of the fixed quantity of liquid fuel has been injected and already passed the measurement position, the gas jet at the later period of the injection can maintain a high velocity due to the reduced gas-liquid momentum transfer. Similarly, no difference was found in the time-resolved decay of the gas flow velocity at different fuel-air injection intervals and the gas velocity showed a monotonic decreasing curve with the sampling time. When the axial sampling position was 30 mm, the gas flow velocity first increases and then gradually decreases with time, as shown in Fig. 14(c). This observation suggests a time-dependence of local gas flow velocity a $x = 30$ mm. When the position moves away from the nozzle, the gas flow velocity continuously decreases with the sampling time. This indicates that the gas flow velocity along the spray axis not only varies with time but also is affected by the sampling position. The gas flow velocity decreases with time at different radial positions. A moderate dependence of $U_g/U_{g,\ Bin\ No.\ 1}$ with radial positions is observed.

4.7. Turbulence intensity characteristics

It is well known that the level of turbulence in the geometry of air-assisted atomization contributes to atomization [36]. The gas-phase turbulence levels in the spray were estimated by using the tracer droplet velocities to approximate gas flow motion. Calculations were based on the corresponding root-mean-square (r.m.s.) of local fluctuating velocity u' and the mean velocity to get the turbulence intensity characteristics τ, as [32]

$$\tau = \frac{u'}{U_g} \tag{9}$$

Fig. 15 shows the gas-phase turbulence intensity under different operating conditions. Air injection duration and fuel-air injection intervals hardly affect the local turbulence intensity, which is close to a constant value between 0.2 and 0.3 and hardly changes with sampling time.

However, the spatial sampling location was found to have a significant effect on the turbulence intensity. In this respect, the turbulence intensity increases significantly with the axial distance from nozzle as well as radial distance from spray axis. In addition, the gradient of the turbulence intensity increase in the radial direction is also more pronounced. To explain this variation, we present the mean flow and r.m.s. of fluctuating velocity as a function of axial positions and various radial positions, as seen in Fig. 16. The mean velocity profiles in Fig. 16 show that the gas flow velocity decelerates in both axial and radial directions. However, the gradient of the velocity decrease in the radial direction is steeper than that in the axial direction under both Bin No. 2 and Bin No. 4. This is because the spray center has little exposure to surrounding ambient gas. In addition, it is interesting to notice a nearly constant fluctuating velocity for different spatial positions but a slight decrease from Bin No. 2 to Bin No. 4. Therefore, the spatial variation of turbulence intensity is dominated by the mean velocity profile of gas flow within spray field. The correlation between mean velocity and turbulence intensity of gas phase implies that the dissipation of the gas jet momentum transfers to turbulence energy of gas phase within the spray field [32].

4.8. Droplet-gas slip velocity

The gas-liquid two-phase jet is characterized by the accompanying gas-phase flow around the liquid droplet. The mean slip velocity between droplet and surrounding gas flow is calculated by

$$U_{slip} = \overline{U} - U_g \tag{10}$$

where $\overline{U}$ is the arithmetic mean velocity of sampling droplets. According to the magnitude of the mean slip velocity between the droplet and gas flow, the downstream evolution of droplet motion is divided into three

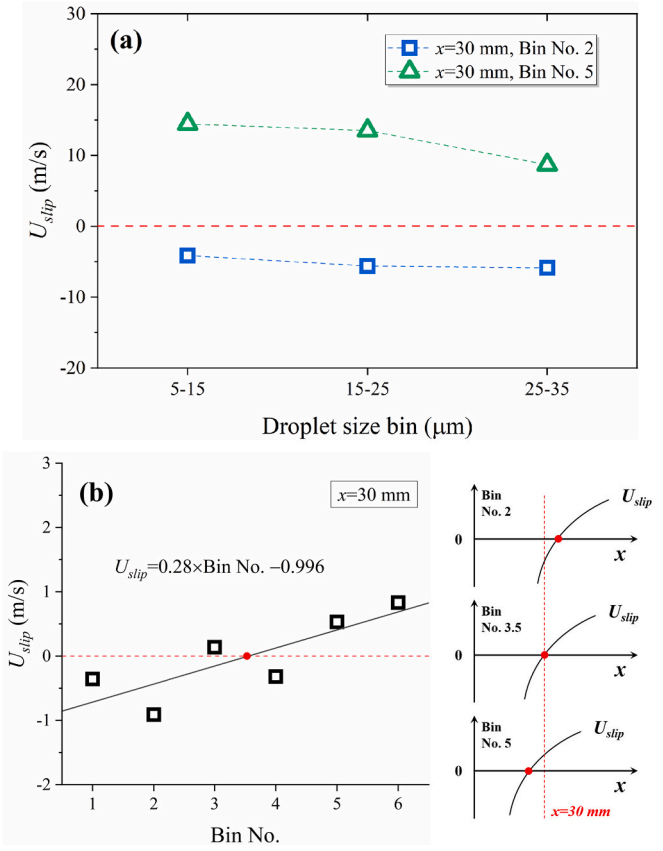

Fig. 19. (a) Mean slip velocity of Bin No. 2 and Bin No. 5 at $x = 30$ mm, (b) time-resolved mean slip velocity evolution and its linear fitting at $x = 30$ mm. The time dependence of the zero point of the mean slip velocity is shown on the right side.

regions [44], as seen in Fig. 17. In the Region I, i.e. the near-nozzle field, droplets are moving at lower velocities than the surrounding gas flow and are continuously accelerated. When the droplet is accelerated to the gas flow velocity, the slip velocity comes to a zero point ($U_{slip} = 0$). However, the droplet will keep accelerating due to its own inertia and lead to overshoot, see Region II. After reaching the maximum overshoot velocity, the droplet decelerates until it approaches the surrounding gas flow velocity in Region III.

Fig. 18(a-b) shows the time-resolved droplet-gas mean slip velocity under different injection control parameters. An almost positive U_{slip} is observed regardless of both air injection duration and fuel-air injection interval. When the axial sampling position is $x = 30$ mm, the U_{slip} appears to be negative at Bin No. 1–2, increases to near zero at Bin No. 3–4, and eventually becomes positive at Bin No. 5–6, as seen in Fig. 18(c). With the increasing of axial position, the U_{slip} becomes positive and is positively correlated with x. According to the analysis of Lasheras and his co-workers [44] on the evolution of the slip velocity on the axis of the gas-liquid two-phase jet, it is suggested that the zero point of the slip velocity in this study is close to $x = 30$ mm. Analogically, the zero point of the slip velocity in radial direction is logically available and expected to be close to $r = 6$ mm, see in Fig. 18(d). However, it should be noted that U_{slip} tends to decrease with radial position away from the spray axis. Therefore, an enclosed surface of $U_{slip} = 0$ with the spray contour is believed to exist and to approximately cross the spatial locations of $x = 30$ mm, $r = 0$ mm and $x = 50$ mm, $r = 6$ mm.

Since the mean slip velocity under the measurement position of $x = 30$ mm presents a distinct time-resolved variation, the sampled droplets within the time bin of negative slip velocity (Bin No. 2) and positive slip velocity (Bin No. 5) are chosen to further analyze the effect of droplet size on the mean slip velocity. The droplet sizes are classified into three size bins: 5–15 μm, 15–25 μm and 25–35 μm. The slip velocities based on various droplet size bins are given in Fig. 19(a). At Bin No. 2, the mean slip velocities of all size bins are all less than zero, which proves that all the sampled droplets regardless of their size are moving with the velocities lower that of surrounding gas flow. At Bin No. 5, the mean slip velocity between droplets from all size bins and gas flow is greater than zero. However, a slight decreasing trend of U_{slip} as function of droplet size can be found for both positive and negative slip velocity, which may be attributed to the fact that small droplets are more likely to react quickly to the surrounding flow and therefore to be accelerated.

According to above discussion, we have noticed that the zero point of the slip velocity on the spray axis is close to $x = 30$ mm. Meanwhile, the mean slip velocity is seen to increase slightly with sampling time (i.e., Bin No.) and thus can be fitted with a linear function of $U_{slip} = 0.28 \times Bin\ No. - 0.996$, as outlined in Fig. 19(b). The horizontal intercept, which is the corresponding zero point of the slip velocity, is calculated to be approximately 3.5. This linear relationship indicated that the droplet-gas slip velocity at $x = 30$ mm is negative at Bin No. 1–3 and increases to positive at Bin No. 4–6. Therefore, a time-varying zero point of slip velocity can be inferred for this intermittent air-assisted spray. That is, the zero point of the slip velocity is far away from the nozzle exit at the beginning of spray and gradually moves toward the nozzle exit as the spraying continues. The potential correlation between the zero point of mean slip velocity and Bin No. is illustrated on the right side of Fig. 19 (b). This time dependence of zero point of mean slip velocity may not exist for continuous and steady jets or sprays but is reasonably expected for intermittent sprays due to their inherently unsteady behaviors and characteristics.

5. Conclusions

In this study, a pulse-worked air-assisted injector was used to generate twin-fluid intermittent spray. A time bin method for sampling time equalization is employed to investigate the time-resolved spray microscopic characteristics and droplet behaviors measured by PDPA. The main findings are summarized as follows.

1. The droplet diameter range is found to be generally independent of air injection duration and Bin No. while droplet velocity is determined by these two parameters. At $T_a \leq 1.0$ ms, the droplet velocity decays rapidly during the late sampling period (Bin No. 5–6) as a result of nozzle closure, which is absent for the cases of $T_a \geq 2.0$ ms where the droplet can be further accelerated by the gas jet. This further acceleration leads to a decreasing SMD while accelerating droplets.
2. Within a certain range, the fuel-air injection interval did not render a notable impact on the spray characteristics, droplet and surrounding gas flow behavior. Droplet SMD shows no variation with sampling time but an increasing function of axial sampling position due to droplet coalescence in spray far-field. The variation of droplet velocity is more pronounced compared to droplet SMD as the sampling position moves from spray axis to outer region.
3. The gas flow velocity exhibits a continuous acceleration with sampling time at $T_a \geq 2.5$ ms. A moderate correlation between axial as well as radial sampling positions and gas flow velocity decay can be observed, but the transition of the gas flow velocity to accelerate and then decelerate with time at $x = 30$ mm should be noted. Estimation of gas flow turbulence intensity indicates a prominent radial sampling position dependence, which is mainly attributed to the rapid attenuation of the gas flow velocity away from the spray axis.
4. The zero point of mean droplet-gas slip velocity within the spray field is close to $x = 30$ mm, $r = 0$ mm in the axial direction and $x = 50$ mm, $r = 6$ mm in the radial direction. The effects of time bin size (ΔT_{bin}) employed to divide the sampling time on spray microscopic characteristics were estimated, and the results indicates that ΔT_{bin} has no

influences on the statistical results of the spray characteristics including the droplet SMD, mass-averaged velocity, local gas flow velocity decay profile and turbulent intensity.

A few important issues merit future attention. High spatial resolution droplet measurements are necessary for further full-field characterization of the time-resolved properties of intermittent air-assisted sprays. The zero point of mean slip velocity at $x = 30$ mm is not a constant value but moves progressively toward the nozzle with sampling time, which has not been revealed in previous studies, but will certainly contribute to our further understanding of the underlying physics and model investigation of intermittent spray emerging from pulsed air-assisted injector.

Declaration of Competing Interest

None.

Acknowledgments

The authors would like to acknowledge the research grant received from the National Natural Science Foundation of China (grant no. 51806013), Foundation research funds of the Ministry of Industry and Information Technology (grant no. WDZC-2019-JGKK-02 and JCKY2019602D018), and Beijing Institute of Technology Research Fund Program for Young Scholars (grant no. 2020CX04047).

References

[1] L. Bayvel, Liquid Atomization, CRC Press, 1993.
[2] A. Saha, J.D. Lee, S. Basu, R. Kumar, Breakup and coalescence characteristics of a hollow cone swirling spray, Phys. Fluids 24 (2012), 124103.
[3] P.-C. Chen, W.-C. Wang, W.L. Roberts, T. Fang, Spray and atomization of diesel fuel and its alternatives from a single-hole injector using a common rail fuel injection system, Fuel 103 (2013) 850–861.
[4] P. Sharma, T. Fang, Spray and atomization of a common rail fuel injector with non-circular orifices, Fuel 153 (2015) 416–430.
[5] X. Wang, Z. Huang, O.A. Kuti, W. Zhang, K. Nishida, Experimental and analytical study on biodiesel and diesel spray characteristics under ultra-high injection pressure, Int. J. Heat Fluid Flow 31 (2010) 659–666.
[6] M. Zaremba, L. Weiß, M. Malý, M. Wensing, J. Jedelský, M. Jícha, Low-pressure twin-fluid atomization: effect of mixing process on spray formation, Int. J. Multiphase Flow 89 (2017) 277–289.
[7] S. Balachandar, J.K. Eaton, Turbulent dispersed multiphase flow, Annu. Rev. Fluid Mech. 42 (2009) 111–133.
[8] X. Jiang, G.A. Siamas, K. Jagus, T.G. Karayiannis, Physical modelling and advanced simulations of gas–liquid two-phase jet flows in atomization and sprays, Prog. Energy Combust. Sci. 36 (2010) 131–167.
[9] M. Mlkvik, J. Jedelsky, H.P. Karbstein, V. Gaukel, Spraying of viscous liquids: influence of fluid-mixing mechanism on the performance of internal-mixing twin-fluid atomizers, Appl. Sci. 10 (2020) 5249.
[10] H. Wu, Z. Zhang, X. Wei, F. Zhang, Atomization and droplet dynamics analysis of air-assisted spray under different gas-liquid ratios, in: International Conference on Liquid Atomization and Spray Systems (ICLASS), 2021.
[11] M. Mlkvik, P. Stähle, H.P. Schuchmann, V. Gaukel, J. Jedelsky, M. Jicha, Twin-fluid atomization of viscous liquids: the effect of atomizer construction on breakup process, spray stability and droplet size, Int. J. Multiphase Flow 77 (2015) 19–31.
[12] S.D. Sovani, P.E. Sojka, A.H. Lefebvre, Effervescent atomization, Prog. Energy Combust. Sci. 27 (2001) 483–521.
[13] A. Kourmatzis, A.R. Masri, Air-assisted atomization of liquid jets in varying levels of turbulence, J. Fluid Mech. 764 (2014) 95–132.
[14] M. Zaremba, J. Kozák, M. Malý, L. Weiß, P. Rudolf, J. Jedelský, M. Jícha, An experimental analysis of the spraying processes in improved design of effervescent atomizer, Int. J. Multiphase Flow 103 (2018) 1–15.
[15] J. Jedelsky, M. Jicha, J. Slama, J. Otahal, Development of an effervescent atomizer for industrial burners, Energy Fuel 23 (2009) 6121–6130.
[16] A.H. Lefebvre, Twin-fluid atomization: factors influencing mean drop size, Atom. Sprays 2 (1992) 101–119.
[17] Z. Li, Y. Wu, H. Yang, C. Cai, H. Zhang, K. Hashiguchi, K. Takeno, J. Lu, Effect of liquid viscosity on atomization in an internal-mixing twin-fluid atomizer, Fuel 103 (2013) 486–494.
[18] S. Wachter, T. Jakobs, T. Kolb, Experimental investigation on the influence of system pressure on resulting spray quality and jet breakup applying pressure adapted twin-fluid nozzles, Int. J. Multiphase Flow 125 (2020), 103189.
[19] S. Wachter, T. Jakobs, T. Kolb, Towards system pressure scaling of gas assisted coaxial burner nozzles – an empirical model, Appl. Energy Combus. Sci. 5 (2021), 100019.
[20] F.A. Hammad, K. Sun, Z. Che, J. Jedelsky, T. Wang, Internal two-phase flow and spray characteristics of outside-in-liquid twin-fluid atomizers, Appl. Therm. Eng. 187 (2021), 116555.
[21] Z. Kang, Q. Li, J. Zhang, P. Cheng, Effects of gas liquid ratio on the atomization characteristics of gas-liquid swirl coaxial injectors, Acta Astron. 146 (2018) 24–32.
[22] T.D. Fansler, S.E. Parrish, Spray measurement technology: a review, Meas. Sci. Technol. 26 (2014), 012002.
[23] Y. Zhao, X. He, M. Li, K. Yao, Experimental investigation on spray characteristics of aircraft kerosene with an external-mixing atomizer, Fuel Process. Technol. 209 (2020), 106531.
[24] S. Yokoi, S. Sugawara, R. Sagawa, Y. Saito, Y. Matsushita, H. Aoki, Experimental investigation of atomization and combustion characteristics of high-pressure pulse sprays, Fuel Process. Technol. 148 (2016) 269–275.
[25] J. Tian, M. Zhao, W. Long, K. Nishida, T. Fujikawa, W. Zhang, Experimental study on spray characteristics under ultra-high injection pressure for DISI engines, Fuel 186 (2016) 365–374.
[26] H.S. Sim, N. Maes, L. Weiss, L.M. Pickett, S.A. Skeen, Detailed measurements of transient two-stage ignition and combustion processes in high-pressure spray flames using simultaneous high-speed formaldehyde PLIF and schlieren imaging, Proc. Combust. Inst. 38 (2021) 5713–5721.
[27] W. Huang, H. Gong, S. Moon, J. Wang, K. Murayama, H. Taniguchi, T. Arima, A. Arioka, Y. Sasaki, Nozzle tip wetting in GDI injector at flash-boiling conditions, Int. J. Heat Mass Transf. 169 (2021), 120935.
[28] H. Gao, F. Zhang, S. Wang, H. Wu, Z. Wang, Effect of characteristic parameters on the magnetic properties of voice coil motor for direct fuel injection in gasoline engine, Energy Proc. 158 (2019) 4184–4189.
[29] H. Wu, F. Zhang, Z. Zhang, H. Gao, A simulation study of static electromagnetic characteristics of voice coil motor injector, IFAC-PapersOnLine 54 (2021) 494–499.
[30] H. Wu, F. Zhang, Z. Zhang, H. Cui, Research on Performance of Pulsed Twin-fluid Injector and Its Application on a Spark Ignition UAV Engine, SAE Technical Paper, 2021 (2021-2001-0651).
[31] Z. Wang, C. Jiang, H. Xu, M.L. Wyszynski, Macroscopic and microscopic characterization of diesel spray under room temperature and low temperature with split injection, Fuel Process. Technol. 142 (2016) 71–85.
[32] S. Moon, Y. Gao, J. Wang, K. Fezzaa, T. Tsujimura, Near-field dynamics of high-speed diesel sprays: effects of orifice inlet geometry and injection pressure, Fuel 133 (2014) 299–309.
[33] S. Moon, T. Li, K. Sato, H. Yokohata, Governing parameters and dynamics of turbulent spray atomization from modern GDI injectors, Energy 127 (2017) 89–100.
[34] Z. Feng, C. Tang, Y. Yin, P. Zhang, Z. Huang, Time-resolved droplet size and velocity distributions in a dilute region of a high-pressure pulsed diesel spray, Int. J. Heat Mass Transf. 133 (2019) 745–755.
[35] H. Wu, F. Zhang, Z. Zhang, H. Gao, Experimental investigation on the spray characteristics of a self-pressurized hollow cone injector, Fuel 272 (2020), 117710.
[36] A. Kourmatzis, P.X. Pham, A.R. Masri, Air assisted atomization and spray density characterization of ethanol and a range of biodiesels, Fuel 108 (2013) 758–770.
[37] M. Manish, S. Sahu, Droplet clustering and local spray unsteadiness in air-assisted sprays, Exp. Thermal Fluid Sci. 100 (2019) 89–103.
[38] H. Gao, F. Zhang, Z. Zhang, S. Wang, H. Wu, Trajectory deviation of target jet of air-assisted spray under different conditions, Fuel 249 (2019) 252–263.
[39] H. Wu, F. Zhang, Z. Zhang, Droplet breakup and coalescence of an internal-mixing twin-fluid spray, Phys. Fluids 33 (2021), 013317.
[40] H. Wu, F. Zhang, Z. Zhang, Fundamental spray characteristics of air-assisted injection system using aviation kerosene, Fuel 286 (2021), 119420.
[41] H. Wu, F. Zhang, Z. Zhang, Z. Guo, W. Zhang, H. Gao, On the role of vortex-ring formation in influencing air-assisted spray characteristics of n-heptane, Fuel 266 (2020), 117044.
[42] A. Urbán, A. Groniewsky, M. Malý, V. Józsa, J. Jedelský, Application of big data analysis technique on high-velocity airblast atomization: searching for optimum probability density function, Fuel 273 (2020), 117792.
[43] S.K. Soni, P.S. Kolhe, Liquid jet breakup and spray formation with annular swirl air, Int. J. Multiphase Flow 134 (2021), 103474.
[44] J.C. Lasheras, E. Villermaux, E.J. Hopfinger, Break-up and atomization of a round water jet by a high-speed annular air jet, J. Fluid Mech. 357 (1998) 351–379.
[45] S. Sahu, Y. Hardalupas, A.M.K.P. Taylor, Droplet–turbulence interaction in a confined polydispersed spray: effect of droplet size and flow length scales on spatial droplet–gas velocity correlations, J. Fluid Mech. 741 (2014) 98–138.
[46] V. Ferrand, R. Bazile, J. Borée, G. Charnay, Gas–droplet turbulent velocity correlations and two-phase interaction in an axisymmetric jet laden with partly responsive droplets, Int. J. Multiphase Flow 29 (2003) 195–217.
[47] J. Jedelsky, M. Maly, N. Pinto del Corral, G. Wigley, L. Janackova, M. Jicha, Air–liquid interactions in a pressure-swirl spray, Int. J. Heat Mass Transf. 121 (2018) 788–804.
[48] F. Li, H. Qi, C. You, Phase Doppler anemometry measurements and analysis of turbulence modulation in dilute gas–solid two-phase shear flows, J. Fluid Mech. 663 (2010) 434–455.
[49] E.K. Longmire, J.K. Eaton, Structure of a particle-laden round jet, J. Fluid Mech. 236 (1992) 217–257.
[50] F. Prevost, J. Boree, H.J. Nuglisch, G. Charnay, Measurements of fluid/particle correlated motion in the far field of an axisymmetric jet, Int. J. Multiphase Flow 22 (1996) 685–701.